

Technische Universität München  
Fakultät für Physik  
Ludwig-Maximilians-Universität München  
Fakultät für Physik



Thesis in the Master Degree Course  
Theoretical and Mathematical Physics

# **Anomalous Quantum Oscillations in a Heterostructure of Graphene on a Proximate Quantum Spin Liquid**

Valentin Leeb

March 29, 2021

Advisor/ Supervisor: Prof. Dr. J. Knolle  
Second referee: Prof. Dr. M. Knap  
Date of the oral exam: April 9, 2021

## Abstract

Quantum oscillation measurements are a standard tool to investigate the electronic structure of metallic materials. Recent magnetotransport measurements in  $\alpha$ -RuCl<sub>3</sub>-graphene heterostructures, in which the insulating  $\alpha$ -RuCl<sub>3</sub> layer is believed to be in a Kitaev quantum spin liquid state, showed an anomalous temperature dependence of the quantum oscillations, going beyond the standard Lifshitz–Kosevich description. This thesis develops a theory of *anomalous quantum oscillations* in a Kitaev–Kondo model in which the spins of the itinerant graphene electrons interact with the Kitaev spins of  $\alpha$ -RuCl<sub>3</sub> via a Kondo interaction. For a large parameter regime a heavy Fermi liquid phase is realized and an effective low energy model thereof is constructed. From this, an analytic formula for the magnetization is derived which explains the non-Lifshitz–Kosevich behavior and is consistent with previous *ab-initio* calculations. The scenario suggests that the former neutral Majorana fermions of the Kitaev quantum spin liquid have acquired charge by the Kondo hybridization with the graphene Dirac electrons. Furthermore the mechanism is applicable beyond the specific example of  $\alpha$ -RuCl<sub>3</sub>-graphene heterostructures. The results of this thesis have been published in ref. [\[1\]](#).



# Acknowledgments

First, I would like to thank Johannes Knolle for his advice in numerous meetings and for giving me the possibility to publish the results together with him and others. I would also like to thank my collaborators Katharina Polyudov, Sananda Biswas, Roser Valentí and Marco Burghard for sharing their knowledge with me and helpful discussions.

Furthermore, I want to thank Markus Gail, Josef Wilsher, Stefan Birnkammer and Ida Sachse for proofreading this thesis.

Finally, I am very thankful for my parents who have always supported me and helped me out with advice.



# Contents

<b>1</b>	<b>Introduction</b>	<b>1</b>
<b>2</b>	<b>The de Haas–van Alphen Effect in the Two-dimensional Fermi Liquid</b>	<b>3</b>
2.1	Qualitative Treatment	3
2.2	Peierls Substitution	5
2.3	Landau Levels in the Two-dimensional Fermi Liquid	6
2.4	Self-Energy and Impurity Scattering	7
2.5	Thermodynamic Potential and Magnetization	8
<b>3</b>	<b>Anomalous Quantum Oscillations in a <math>\alpha</math>-RuCl<sub>3</sub>-Graphene Heterostructure</b>	<b>10</b>
3.1	Quantum Spin Liquids	10
3.2	Kitaev’s Honeycomb Model	11
3.3	Kitaev Materials	12
3.4	From the Kitaev–Kondo Model to an Effective Low Energy Hamiltonian	13
3.4.1	The Kitaev–Kondo Model	13
3.4.2	Majorana Representation	14
3.4.3	Parton Mean-Field Theory	15
3.4.4	Back Transformation to Complex Fermions	17
3.4.5	Effective Low Energy Model	19
3.5	Landau Level Structure and Quantum Oscillations	21
3.5.1	Magnetic Field and Landau Levels	21
3.5.2	Poles of the Green’s function	23
3.5.3	The Decoupled Limit	24
3.5.4	The Limit of the $\alpha$ -RuCl <sub>3</sub> -Graphene Heterostructure	25
3.6	Comparison to the Experimental Data	28
3.6.1	Experimental Samples	28
3.6.2	Fitting	29
3.6.3	Discussion of the Fits	31
3.6.4	Exponential Suppression of the QOs within the Hybridization Region	33
3.7	Discussion	33
<b>4</b>	<b>Conclusion</b>	<b>35</b>
	<b>Bibliography</b>	<b>37</b>

*Contents*

<b>List of Figures</b>	<b>41</b>
<b>List of Tables</b>	<b>42</b>
<b>A Derivation of the Generalized LK Formula</b>	<b>43</b>
<b>B Additional Material for Chapter 3</b>	<b>47</b>
B.1 Sublattice Symmetry Breaking Term . . . . .	47
B.2 Fourier Spectra of Sample B and C . . . . .	49
B.3 Additional Fits and Fitting Parameters . . . . .	50





# Chapter 1

## Introduction

Understanding electronic behavior of quantum materials has been one of the biggest and most active fields in Physics. The interest in this topic is driven not only by curiosity, but also by its importance for modern electronics. Even though there are many open questions for different materials, engineers have successfully exploited electronic properties to construct numerous different electronic devices, starting with the prominent transistor in the 1940's. In the semiconductor industry the critical dimensions of transistor gates are meanwhile as small as 5 nm. Less energy consumption and overheating problems, higher performance, and cost reduction push to reduce structures further, making quantum effects relevant for commercial technologies as well.

For many applications the electronic properties of metals are important. These properties are governed by the metal's band structure and Fermi surface. Hence various theoretical, numerical and experimental methods to determine these properties have been developed. Famously, quantum oscillation (QO) measurements have been a standard tool for investigating electronic properties of metallic materials since the late 1950's. By measuring the frequency of the oscillations it is possible to infer the size of the metal's Fermi surface, whereas the measurement of the temperature decay allows the determination of the effective mass of the electrons. One reason for the success of QO measurements is that nearly all discovered materials follow the same behavior — the venerable Lifshitz–Kosevich (LK) theory [2]. Since the completion of the standard theory for QOs by Lifshitz and Kosevich in 1956, one by one all metals have followed its description. Starting with the seminal discovery of QO in bismuth by de Haas and van Alphen in 1930 [3], through the first observation in copper by Schoenberger in 1959 up to modern materials like cuprate high temperature superconductors, no material has shown robust deviations to the LK paradigm until a few years ago [4, 5].

With the advent of strongly correlated quantum materials in condensed matter physics in the last decades the question arose if the LK theory has limitations and if so, how it could be extended. Still it was a surprise when experimentalists observed QOs with a non-LK temperature decay in the correlated insulator  $\text{SmB}_6$  [6, 7]. Already the observation of QOs in an insulator, which does not have a Fermi surface, is at odds with the canonical theory of QOs, persistent for more than 50 years. The non-LK temperature decay is even more astonishing. This exciting new phenomena has lead to the discovery

## Chapter 1 Introduction

of *anomalous QOs* in other materials [8, 9] and several theoretical explanations going beyond the LK theory [10-15].

This thesis introduces a theoretical minimal model to explain recent measurements which show *anomalous QOs* with a non-LK amplitude in a heterostructure of graphene on  $\alpha\text{-RuCl}_3$ . Such heterostructures have been recently synthesized [16] and are of great interest as the  $\alpha\text{-RuCl}_3$  layer is believed to be in a quantum spin liquid state [16, 17]. Hence QO measurements can be viewed as a probe to determine the state of matter. The microscopic theory is based on the electronic behavior of graphene and the quantum spin liquid behavior of  $\alpha\text{-RuCl}_3$  which are coupled via a Kondo spin interaction. I will show how the interplay of itinerant graphene electrons and the fractionalized spin excitations will lead to QOs with an unconventional non-LK amplitude. In order to validate the theoretical findings, I will directly compare them to recent experimental measurements.

# Chapter 2

## The de Haas–van Alphen Effect in the Two-dimensional Fermi Liquid

### 2.1 Qualitative Treatment

Before diving deeply into the theory of QOs, first a qualitative explanation is given how QOs emerge in metallic materials. The presented central formulas were initially derived semi-classically [2, 18] and are not proven here, but benchmarked by a quantum mechanical derivation in the two-dimensional Fermi liquid. Hereinafter the constants  $\hbar$ ,  $k_B$  and  $c$  are set to 1, but reinstated in quantities which are compared to experimental values.

The normal state of most metals can be described by Fermi liquid theory. Within Fermi liquid theory the quasiparticles, arising from the weakly interacting electrons, are viewed as free fermions. Assuming a translational invariant system, the quasiparticles occupy momentum eigenstates which are distributed uniformly in momentum space. If the metal is exposed to a magnetic field  $B$ , the eigenstates in the plane perpendicular to the field collapse on certain energy levels  $E_l$ , so called Landau Levels (LLs), see fig. 2.1. In contrast the out-of-plane momentum remains untouched, such that the LLs can be imagined as nested cylinders, called Landau tubes, orientated with their axis in field direction. Consecutive LLs differ in energy in units of the cyclotron frequency  $\omega_c = eB/m$ , which is for quadratically dispersive bands inversely proportional to the effective mass of the quasiparticles  $m$  and proportional to the magnetic field  $B$ . Each LL is highly degenerate and hosts a macroscopic number of states. At or close to zero temperature all LLs below the Fermi energy  $E_F$  are occupied whereas the LLs above are empty.

The effect of changing the applied magnetic field is the following: An increase of the magnetic field increases the energy difference between the LLs  $\omega_c$  and at the same time LLs become more populated. In consequence the LLs pass through the, at low temperatures sharp, Fermi edge at equal intervals of  $1/B$ . Therefore the density of states at the Fermi energy varies periodically. The density is high while a LL is just passing through the Fermi edge and low in between. Since the density of states at the Fermi energy is a quantity strongly influencing physical observables, it is possible to measure

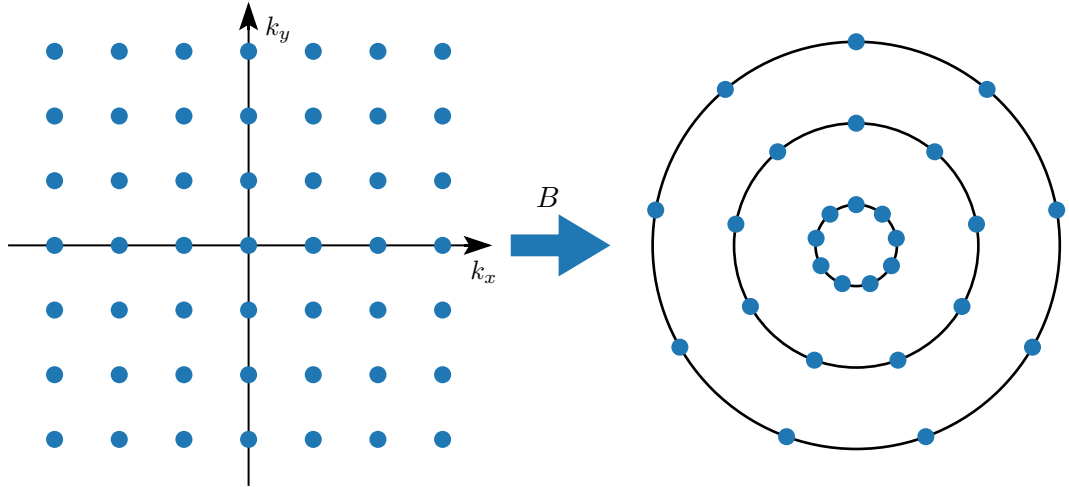


FIGURE 2.1: Schematic depiction of the effect of a magnetic field  $\mathbf{B} \propto e_z$  on the momentum eigenstates in the perpendicular plane. In anisotropic or non-Fermi liquid systems the LLs may be deformed.

these oscillations in several quantities. Oscillations of magnetic quantities, i.e. the magnetization and the susceptibility, are called the de Haas–van Alphen (dHvA) effect, while oscillations of the resistivity are known as the Shubnikov–de Haas (SdH) effect.

The frequency of the dHvA and the SdH oscillations is connected to the geometry of the metal’s Fermi surface. Famously, Onsager’s relation

$$F = \frac{\hbar}{2\pi e} S \quad (2.1)$$

states that the frequency  $F$  is given by the extremal cross section of the Fermi surface  $S$  perpendicular to the magnetic field [18]. Usually also higher harmonics, i.e. integer multiples of the elemental frequency  $F$ , can be observed.

Until now we have considered a highly idealized system which is perfectly clean and exposed to zero temperature which raises the question if the phenomenon of QOs is persistent in real systems. The influence of finite temperature or impurities in the system are to simply blur out the sharp Fermi edge and broaden the LLs. In consequence the sharpness of the QOs and their amplitudes are reduced by universal damping factors.

The universal temperature damping factor is the LK damping factor

$$R_{\text{LK}}(\chi) = \frac{\chi}{\sinh \chi} \quad (2.2)$$

where  $\chi \propto T/B$  can be used to define an effective mass via the cyclotron frequency. Hence the QOs are damped exponentially for sufficiently high temperatures. In experiments it

has been observed that the temperature behavior at large temperatures can be described better, if instead of  $T$  a shifted temperature  $T + T_D$  is used, where  $T_D$  is known as the Dingle temperature. It will transpire that this shift is a result from electrons scattering on the system's impurities, implying a finite quasiparticle relaxation time  $\tau \sim 1/T_D$ . The finite relaxation time broadens the LLs in a Lorentzian fashion and reduces the amplitude of the QOs by the Dingle reduction factor

$$R_D = \exp\left(-2\pi^2 \frac{T_D}{\omega_c}\right). \quad (2.3)$$

These findings are universal in the sense that nearly all metals exhibit the SdH effect and the dHvA effect and are damped by the Dingle and the LK factor.<sup>[1]</sup> Within the standard LK theory there is in fact no qualitative difference between the behavior of the resistivity and quantities derived from the thermodynamic potential, like e.g. the magnetization [4]. For theoretical calculations this is of very convenient, since the resistivity is usually easier to measure experimentally especially in two-dimensional systems, while theoretical calculations and simulations are mostly easier for thermodynamic quantities. For the calculation of transport quantities additional assumptions on the scattering channels need to be made.

## 2.2 Peierls Substitution

Throughout this thesis the models will be exposed to a magnetic field  $\mathbf{B}$  pointing in  $z$ -direction. Within minimal coupling this can be described by forwarding the kinetic momentum operator  $\mathbf{p}$  to the canonical momentum operator  $\mathbf{p} \rightarrow \mathbf{p} - e\mathbf{A}$ . The vector potential  $A = -(By, 0, 0)^T$  is fixed by the Landau gauge. Inserting the kinetic momentum operator, leads to the *quantization rules*

$$\begin{aligned} p_x \rightarrow p_x + eBy &= \frac{1}{\ell_B^2}(y - y_0) = \frac{1}{\sqrt{2}\ell_B} (\hat{a}^\dagger + \hat{a}) \\ p_y \rightarrow p_y &= p_{y-y_0} = \frac{i}{\sqrt{2}\ell_B} (\hat{a}^\dagger - \hat{a}) \end{aligned} \quad (2.4)$$

where  $\ell_B = \sqrt{\hbar/eB}$  is the magnetic length. The operators  $\hat{a}$  and  $\hat{a}^\dagger$  are the ladder operators of a quantum harmonic oscillator which is located at  $y_0 = -p_x \ell_B^2$ .

All systems considered in this thesis feature translational invariance without the external magnetic field, such that  $\mathbf{p}$  may be replaced by its eigenvalue  $\mathbf{k}$ . Note that the Landau gauge breaks translational invariance in  $y$ -direction, such that  $k_y$  is not a good a quantum number anymore.

In the literature the quantization of the former continuous momenta is known as *quantizing magnetic field*. The physical consequences are explained in the next section.

<sup>1</sup>For some exotic systems the constant in the Dingle and the LK factor may change but their fundamental form remains valid.

### 2.3 Landau Levels in the Two-dimensional Fermi Liquid

In this section the effect of a quantizing magnetic field on a two-dimensional Fermi liquid is evaluated. Its Hamiltonian reads

$$H = \int d\mathbf{r} \phi(\mathbf{r})^\dagger \frac{\mathbf{p}^2}{2m} \phi(\mathbf{r}) \quad (2.5)$$

where  $\mathbf{p}$  is the momentum operator,  $m$  is the effective mass of the quasiparticles and  $\phi$  are their quantum field operators.<sup>[2]</sup> Without a magnetic field, this simple Hamiltonian can be solved by Fourier transformation

$$\phi(\mathbf{k}) = \frac{1}{2\pi} \int d\mathbf{r} e^{-i\mathbf{k}\mathbf{r}} \phi(\mathbf{r}) \quad (2.6)$$

to get

$$H = \int d\mathbf{k} \frac{\mathbf{k}^2}{2m} \phi(\mathbf{k})^\dagger \phi(\mathbf{k}). \quad (2.7)$$

The result are the momentum eigenstates shown in the left part of fig. 2.1 and the usual quadratic energy dispersion.

Applying the quantization rules eq. 2.4, the Hamiltonian inside a magnetic field reads

$$H = \omega_c \int dy dk_x \phi(k_x, y)^\dagger \left( \hat{a}^\dagger \hat{a} + \frac{1}{2} \right) \phi(k_x, y) \quad (2.8)$$

with the cyclotron frequency  $\omega_c = eB/m = (m\ell_B^2)^{-1}$  and the fields were Fourier transformed in  $x$ -direction, but not in the  $y$ -direction, due the broken translational invariance in  $y$ -direction. Next we introduce the quantized fields

$$\phi_l(k_x) = \int dy \psi_l^*(y - y_0) \phi(k_x, y) \quad (2.9)$$

which is equivalent to  $\phi(k_x, y) = \sum_l \psi_l(y - y_0) \phi_l(k_x)$ . Here  $\psi_l(y - y_0)$  denote the orthonormal eigenstates of the quantum harmonic oscillator located at  $y_0$  with the properties  $\hat{a}\psi_l = \sqrt{l}\psi_{l-1}$  and  $\hat{a}^\dagger\psi_l = \sqrt{l+1}\psi_{l+1}$ . The transformation in eq. 2.9 diagonalizes the Hamiltonian in the LL basis

$$H = \omega_c \int dk_x \sum_l \left( l + \frac{1}{2} \right) \phi_l(k_x)^\dagger \phi_l(k_x). \quad (2.10)$$

The result are equidistant LLs  $E_l = \omega_c(l + 1/2)$ , separated by the cyclotron frequency  $\omega_c$ . The LLs are independent of  $k_x$ . In any physical system the momentum  $k_x$  is quantized by the finite system size, leading to a microscopically high degeneracy

$$N_\Phi = \frac{\Phi}{\Phi_0} = \frac{L_x L_y B}{\Phi_0} \quad (2.11)$$

<sup>2</sup>The dimension of the fields is given by  $[\phi(\{z_i\})] = \prod_i [z_i]^{-1/2}$ , such that  $\int \prod_i dz_i |\phi(\{z_i\})|^2 = 1$  is normalized.

of each LL, which we may express as the number of flux quanta  $\Phi_0 = 2\pi\hbar/e$  trapped inside the system. The degenerate states of each LL only differ by a phase set by  $k_x$ .

In summary the former uniformly distributed momentum eigenstates with paraboloidal energy dispersion collapse on, in energy space equally spaced, ring-shaped LLs, see fig. 2.1. Extending the discussion from two to three dimensions is simple: The  $k_z$  momentum remains unchanged by the magnetic field  $B \propto \hat{e}_z$  such that the energy dispersion in  $z$ -direction does not change. In the simple case of a three-dimensional Fermi liquid the LLs just become cylindrical Landau tubes. The fact that the  $k_z$  momentum keeps its former meaning is also true for more elaborate systems.

## 2.4 Self-Energy and Impurity Scattering

In any actual metal the electrons interact with each other as well as with impurities, being present in all real system. Weak electron interactions only renormalize several system quantities and lead to the quasiparticle picture in Fermi liquid theory that has been used so far. In the following electron interactions are kept weak such that the quasiparticle description remains valid, but additionally impurities are introduced. However the influence of impurity scattering on electron interactions is ignored.

The effect of such impurities can be in lowest order easily included in calculations. A more accurate treatment would require knowledge about the exact interaction potential, for example for charged impurities the Coulomb potential. However, it is for most applications sufficient to assume a simple short-ranged potential. This is due to the fact that the main contribution to the quasiparticle momentum relaxation is made by quasiparticle scattering on the short-range impurities [19].

Mathematically impurities can be treated by adding a disorder potential

$$V = U_0 \sum_{\mathbf{r}_i} \delta(\mathbf{r} - \mathbf{r}_i) \phi(\mathbf{r})^\dagger \phi(\mathbf{r}) \quad (2.12)$$

for one particular configuration of impurities located at  $\mathbf{r}_i$ , to the Hamiltonian. For macroscopic systems the specific microscopic distribution of the impurities is usually irrelevant, since such systems are self-averaging. Their behavior can be characterized by an average over microscopically identical subsystems [20]. This average also restores translational invariance. It is now possible to compute the impurity averaged self-energy  $\Sigma$  within the self-consistent Born approximation, neglecting cross scattering events and multiple ( $> 2$ ) scattering events of the same impurity, see for example ref. [21, p. 266f.] or ref. [20]. The result is

$$\Sigma(i\omega) = -i \frac{\text{sgn}(\omega)}{2\tau} \quad (2.13)$$

where the quasiparticles elastic scattering rate  $\tau$  depends on the strength of the scattering potential and on the density of the impurities. Note that the scattering rate is

connected to the Dingle temperature  $1/2\tau = \pi T_D$  which usually lies at order of a few Kelvin.<sup>3</sup> In general  $\Sigma$  is a complex quantity and its real part only renormalizes the Fermi energy.

## 2.5 Thermodynamic Potential and Magnetization

In the following we will work in the grand canonical ensemble at temperature  $T$  and with a chemical potential  $\mu > 0$ . In order to find observables that oscillate with respect to the magnetic field we need to calculate the grand canonical potential  $\Omega$  which is in fermionic systems given by

$$\Omega = -N_{\Phi} T \sum_l \ln \left( 1 + e^{\frac{\mu - E_l}{T}} \right) \quad (2.14)$$

where the degeneracy of each LL is already summed out. Apart from the fact that an explicit calculation of this sum is very difficult, this formula is not in general applicable. It is only valid for non-interacting fermions, which necessarily have  $\Sigma = 0$ . The more general formula

$$\Omega = -T \operatorname{tr}_{l, \omega_n, k_x, \lambda} (\ln -G^{-1}(i\omega_n)) - T \operatorname{tr}_{l, \omega_n, k_x, \lambda} (G(i\omega_n)\Sigma(i\omega_n)) + \Omega' \quad (2.15)$$

was derived by Luttinger and Ward in 1960 [22] and applies for interacting fermions as well. The trace  $\operatorname{tr}$  extends over all LLs  $l$  starting at  $l = 0$ , all fermionic Matsubara frequencies  $\omega_n = 2\pi T(n+1/2)$ , the trivial quantum number  $k_x$  and all additional quantum numbers in the system  $\lambda$  like e.g. spin or  $k_z$ -momentum. Furthermore

$$G(i\omega_n) = \frac{1}{i\omega_n + \mu - H - \Sigma(i\omega_n)} \quad (2.16)$$

is the full, impurity averaged, finite-temperature Green's function. The last term  $\Omega'$  is given by the Luttinger–Ward functional and does not need to be further specified for this thesis.<sup>4</sup>

From here on usually a specific Hamiltonian is plugged in to continue with the calculation. It is however also possible to proceed with a generic Hamiltonian  $H$  and arrive at a closed expression for  $\Omega$ , see ch. A in the appendix. The resulting formula, referred to as *generalized Lifshitz–Kosevich* formula,

$$\Omega_{\text{osc.}} = N_{\Phi} T \Re \sum_{k=1}^{\infty} \sum_{n=0}^{\infty} \theta(\Re l_n^*) \frac{1}{k} e^{2\pi i k l_n^* \operatorname{sgn}(\Im l_n^*)} \quad (2.17)$$

<sup>3</sup>Although this relation is mathematically correct it does often not hold experimentally [4]. Hence only the Dingle temperature is used in this thesis, as it is the correct quantity for QOs.

<sup>4</sup>In the literature sometimes eq. 2.15 is referred to as Luttinger–Ward functional.

## 2.5 Thermodynamic Potential and Magnetization

was first reported in ref. [23], subsequently employed and benchmarked in ref. [10], and derived in its general form in this thesis, see ch. A. Eq. 2.17 connects the complex poles  $l_n^*$  of the finite-temperature Green's function with the part of the grand canonical potential  $\Omega_{\text{osc.}}$  which oscillates when the magnetic field  $B$  is varied. The generalized LK formula confers the pole  $l_n^*$  physical meaning. Its real part becomes the argument of the oscillating cos terms, while the imaginary part damps the amplitude of these oscillations.

In the following we apply eq. 2.17 to the results from the previous section. The findings were LLs with an energy dispersion  $E_l = \omega_c(l+1/2)$  and the self-energy  $\Sigma(i\omega_n) = -i\pi T_D \text{sgn}(\omega_n)$ . Therefore the Green's function in the two-dimensional Fermi liquid with impurities has only a single pole

$$l_n^* = -\frac{1}{2} + \frac{\mu}{\omega_c} + i \text{sgn}(\omega_n) \frac{|\omega_n| + \pi T_D}{\omega_c}. \quad (2.18)$$

The sum over  $n$  from eq. 2.17 can be performed analytically

$$\sum_{n=0}^{\infty} e^{-2\chi(n+\frac{1}{2})} = \frac{1}{2 \sinh \chi}, \quad (2.19)$$

such that the result is

$$\Omega_{\text{osc.}} = \omega_c \frac{N_{\Phi}}{4\pi^2} \sum_{k=1}^{\infty} \frac{(-1)^k}{k^2} \cos\left(2\pi k \frac{\mu}{\omega_c}\right) R_D^k R_{\text{LK}}\left(2\pi^2 k \frac{T}{\omega_c}\right). \quad (2.20)$$

In eq. 2.20 the Dingle factor eq. 2.3 and the LK damping factor eq. 2.2 with  $\chi = 2\pi^2 k \frac{T}{\omega_c}$  appear as expected. Furthermore the thermodynamic potential oscillates in  $1/B$  with a frequency  $F = S/2\pi e$  where  $S = 2\pi m\mu$  is the size of the Fermi surface. This is the manifestation of Onsager's relation eq. 2.1<sup>5</sup>. As stated before it is also possible to observe the higher harmonics  $k > 1$ , but usually these are strongly suppressed by the Dingle factor. In practice only the first few harmonics can be observed, depending on the purity of the material.

The out-of-plane magnetization, measured in the dHvA effect, can be calculated via  $M = -\partial\Omega_{\text{osc.}}/\partial B$ . After applying the product rule several terms arise, but in most cases they are dominated by the derivative of the cos term which is of the order of  $\mu/\omega_c$  and therefore large. The out-of-plane magnetization has the same main properties as the thermodynamic potential

$$M = -\frac{\mu}{B} \frac{N_{\Phi}}{2\pi} \sum_{k=1}^{\infty} \frac{(-1)^k}{k} \sin\left(2\pi k \frac{\mu}{\omega_c}\right) R_D^k R_{\text{LK}}\left(2\pi^2 k \frac{T}{\omega_c}\right). \quad (2.21)$$

This is the famous LK result as it is stated in ref. [4].

A calculation of magnetotransport quantities would start from Kubo formula and similar integrals must be performed as in the derivation of the generalized LK formula eq. 2.17. In the end the same main features as for the magnetization are found.

<sup>5</sup>In two dimensions the only extremal cross section of the Fermi surface is the Fermi surface itself.

## Chapter 3

# Anomalous Quantum Oscillations in a $\alpha$ - $\text{RuCl}_3$ -Graphene Heterostructure

### 3.1 Quantum Spin Liquids

The field of quantum spin liquids (QSLs) started half a century ago with the resonating valence bond (RVB) state which Anderson proposed as the ground state of an antiferromagnetic spin- $1/2$  Heisenberg model on a triangular lattice [24]. In contrast to ferromagnets, antiferromagnetic models have on non-bipartite lattices very complicated ground states due to the frustration of the spins. The RVB state was envisioned as the superposition of all possible singlet pairings between neighboring spins on the lattice. The state is therefore highly and long-range entangled. Even though Anderson’s conjecture proved not to be correct, it unearthed the importance of frustration to stabilize QSLs.

Over the decades the question “What is a quantum spin liquid?” has evaded a clear answer. A simple but negative definition is the understanding of a QSL as a classical liquid: A spin liquid is a system of interacting spins which do not order, i.e. become a “spin solid”, even at very low or zero temperature. Modern research resolves the lack of a definition mostly by characterizing QSLs by their features. A prominent feature is the presence of an anomalously high degree of entanglement which means, without being too precise, that the ground state is not smoothly connected to a product state [25, 26]. Note that the RVB state is clearly a state exhibiting this feature.

The high amount of entanglement of QSLs states has striking implications. QSL states have the ability to support non-local excitations, i.e. excitations that cannot be created by any local operator, but only by an infinite set of local operators. Nevertheless these excitations behave as sharp quasiparticles with finite energy. Furthermore the non-local excitations are anyons, meaning that they can have fractionalized quantum numbers and non-trivial statistics. Famously the Toric code model, a spin- $1/2$  model, features unexpectedly a fermionic anyon.

Apart from their interesting physics QSLs are explored due to another reason. Simulations of quantum mechanical many-particle systems are often exponentially hard, since the size of the Hilbert space scales exponentially with the system size. A possible

solution, suggested initially by Feynman, is the construction of quantum computer to simulate such systems. However to outperform classical super computers a large amount of error free, logical qubits is needed which is in today's quantum computers much smaller than the number of physical qubits. Kitaev suggested using the anyonic super selection of a QSL to create a fault-tolerant quantum computer [27]. The anyons are due to their non-local nature, stable against local perturbations. Such a *topological quantum computer* could easily push the size of the simulatable system far beyond the current limits. With this ideal in view, a larger community of scientist became interested to find QSL materials as possible candidates for a future topological quantum computer.

The most prominent examples for spin Hamiltonians which host a QSL and are exactly solvable are Kitaev's Toric code model [27] and Kitaev's honeycomb model [28]. The later one will be the basis for the model of this chapter and will be discussed in the next section.

## 3.2 Kitaev's Honeycomb Model

Kitaev's honeycomb model has become a widely studied model in the last years. In the wake of this several detailed introductions have been written and also Kitaev's seminal work [28] is quite pedagogical in the beginning. Referring for details to ref. [28-30], the discussion is kept at a qualitative level here, recapping only the important points which are relevant for the later model, following mostly ref. [29].

The Kitaev model is a spin-1/2 system in which spins are located at the vertices of a two-dimensional honeycomb lattice with lattice vectors  $\mathbf{n}_1$ ,  $\mathbf{n}_2$  and lattice constant  $a$ , see fig. 3.1 (a). The honeycomb lattice consists of two equivalent hexagonal sublattices  $A$ ,  $B$  and three inequivalent bond directions (links)  $x$ ,  $y$  and  $z$  between the vertices.

The spin-1/2 degrees of freedom interact via nearest-neighbor Ising like interactions  $S_i^\alpha S_j^\alpha$  with anisotropic coupling  $K^\alpha$  where the coupling and the Ising interaction directions  $\alpha$  depend on the bond direction  $\alpha = x, y, z$

$$H_K = - \sum_{\langle i,j \rangle_\alpha} K^\alpha S_i^\alpha S_j^\alpha. \quad (3.1)$$

The expression  $\langle i,j \rangle_\alpha$  denotes the  $\alpha$ -link, connecting the two neighbored sites  $i$  and  $j$ . The sum extends over all  $3N$  links where  $N$  is the number of unit cells. The Kitaev interactions between the neighboring spins cannot be satisfied simultaneously, they are frustrated and the system is driven into a QSL phase.

Remarkably this model is exactly solvable [28] and well understood. First it is important to realize that the model features an extensive number of conserved quantities. For each plaquette  $p$  the plaquette operator

$$W_p = \prod_{\langle i,j \rangle_\alpha \in p} S_i^\alpha S_j^\alpha \quad (3.2)$$

commutes with the Hamiltonian and all other plaquette operators. Thus they can be replaced by their eigenvalues  $\pm 1$ . The eigenvalue -1 (+1) is associated with a plaquette that carries a flux (no flux). These flux excitations  $W_p = -1$  turn out to be gapped and static. The macroscopic number of conserved quantities simplifies the problem by restricting the discussion to a given flux sectors which is the set of flux carrying plaquettes. According to Lieb's theorem [31], the ground state flux sector is flux free, i.e.  $W_p = 1$  for all plaquettes.

For a given flux sector the solution proceeds with representing spins by Majorana fermions, known as Kitaev's representation of spins

$$S_j^\alpha = i\chi_j^0\chi_j^\alpha \quad (3.3)$$

where  $\chi_j^\mu$  are real Majorana fermions with  $\{\chi_i^\mu, \chi_j^\nu\} = \delta^{\mu,\nu}\delta_{i,j}$ . The Hamiltonian is then given by

$$H_u = \sum_{\langle i,j \rangle_\alpha} K^\alpha i u_{i,j} \chi_i^0 \chi_j^0 \quad (3.4)$$

with the link variable  $u_{i,j} = i\chi_i^\alpha\chi_j^\alpha$ . At first glance this does not seem like a simplification as we still need to solve a quartic Hamiltonian. However the link variables  $u_{i,j}$  commute among themselves and with the Hamiltonian, such that they can be replaced by their eigenvalues  $\pm 1$ . Therefore the previously quartic Hamiltonian reduces to a non-interacting Majorana hopping Hamiltonian, coupled to a static  $\mathbb{Z}_2$  gauge field  $u_{i,j}$ .<sup>[1]</sup> It can be shown that the product of all link-variables along the edge of a plaquette also gives the plaquette operator  $W_p$ .

Solving the problem in the ground state flux sector is surprisingly easy. Inside the ground state flux sector, we can fix the gauge by choosing  $u_{i,j} = 1$  for  $i \in A$  and  $j \in B$ , such that the system is flux-free and translational symmetric. The Hamiltonian is diagonalized by Fourier transformation. The outcome are dispersing Majorana fermions, which are gapless around the isotropic point  $K^x = K^y = K^z$  and gapped only if  $|K^z| > |K^x| + |K^y|$  or any permutation of thereof. These different parameter regions turn out to be two distinct phases as indicated by the gap closure.

### 3.3 Kitaev Materials

Even though the constructed Hamiltonian of the Kitaev model eq. [3.1] appears at first glance to be a toy model for theorist, a Kitaev term can be present in actual materials. As discussed in detail in ref. [32] the orbitals of transition metal compounds with partially filled  $d$ -orbitals can interact such that the effective low energy Hamiltonian is a spin-only

---

<sup>1</sup>As the experienced readers might know this comes at the cost of enlarging the Hilbert space. The projection to the physical subspace is not further discussed here.

### 3.4 From the Kitaev–Kondo Model to an Effective Low Energy Hamiltonian

Hamiltonian. The interactions between a spin at site  $i$  and a spin at site  $j$  (which are connected by an  $\alpha$ -bond) are then described by so called  $JKTT'$ -models

$$H_{ij} = J_{ij} \mathbf{S}_i \cdot \mathbf{S}_j + K_{ij}^\alpha S_i^\alpha S_j^\alpha + \Gamma_{ij}^\alpha (S_i^\beta S_j^\gamma + S_i^\gamma S_j^\beta) + \Gamma_{ij}^{\alpha'} (S_i^\alpha S_j^\beta + S_i^\alpha S_j^\gamma + S_i^\beta S_j^\alpha + S_i^\gamma S_j^\alpha). \quad (3.5)$$

In addition to the Kitaev interaction  $K$  these materials possess Heisenberg  $J$ , off-diagonal symmetric  $J$  and off-diagonal antisymmetric  $J'$  couplings. Prominent examples with a comparably large Kitaev term include the Iridates  $\text{Na}_2\text{IrO}_3$  and  $\alpha\text{-Li}_2\text{IrO}_3$ , and most importantly for this thesis  $\alpha\text{-RuCl}_3$ .

In  $\alpha\text{-RuCl}_3$  the additional couplings of eq. 3.5 lead to an antiferromagnetic order at low temperatures [33]. Several methods are currently tried to suppress the magnetism and strengthen the Kitaev interaction, including the application of external fields, pressure and doping. A promising way, initially performed in ref. [16], is to proximitize a  $\alpha\text{-RuCl}_3$  layer to a graphene layer to construct a heterostructure. A numerical study based on *ab-initio* density functional theory (DFT) calculations shows that the Kitaev interaction is enhanced by more than 50% compared to bulk  $\alpha\text{-RuCl}_3$  by straining the  $\alpha\text{-RuCl}_3$  layer [17].

Excitingly  $\alpha\text{-RuCl}_3$ -graphene heterostructures have recently been synthesized and the  $\alpha\text{-RuCl}_3$  layer is believed to be a proximate QSL [16, 34]. Magnetotransport measurements of the  $\alpha\text{-RuCl}_3$ -graphene heterostructures have shown quantum oscillations with a non-LK temperature dependent amplitude [34]. The amplitude does not decay monotonously as predicted by eq. 2.2, but features a clear maximum at  $\approx 7\text{K}$ . The quest of this chapter will be to find a possible explanation for this non-canonical behavior which is based on a Kitaev behavior of the  $\alpha\text{-RuCl}_3$  layer. Although the theory will be engineered for a  $\alpha\text{-RuCl}_3$ -graphene heterostructure, it will as well be applicable to any other heterostructure of graphene and a Kitaev material and even for other heterostructures.

## 3.4 From the Kitaev–Kondo Model to an Effective Low Energy Hamiltonian

### 3.4.1 The Kitaev–Kondo Model

A simple model which can explain the basic effects in a  $\alpha\text{-RuCl}_3$ -graphene heterostructure is a Kitaev–Kondo model, schematically depicted in fig. 3.1 (b). In this model spins and local-moment conduction electrons live on a two-dimensional honeycomb lattice. The conduction electrons perform nearest-neighbor hoppings on the lattice with hopping amplitude  $t$  eq. 3.6. This is the well known tight-binding description for graphene [35].

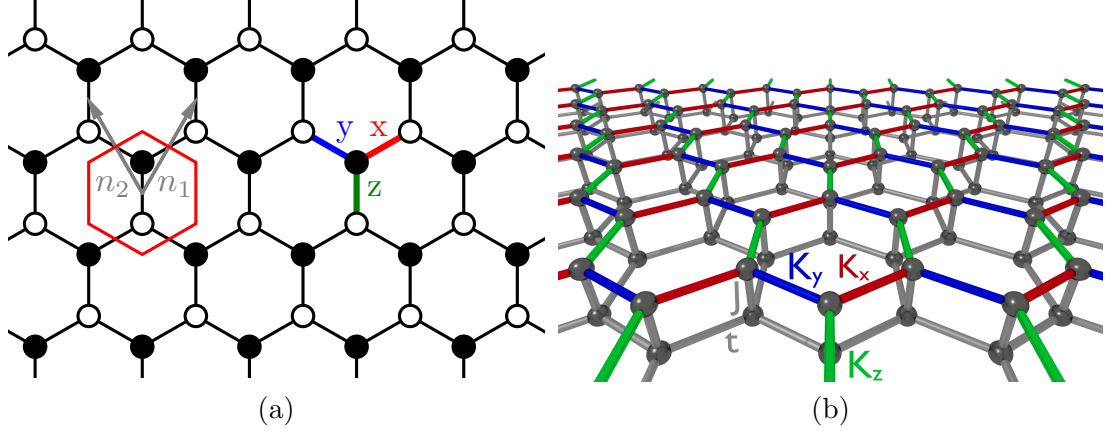


FIGURE 3.1: Panel (a) shows the two-dimensional honeycomb lattice with lattice vectors  $\mathbf{n}_1$ ,  $\mathbf{n}_2$ , the unit cell bordered in red and the three inequivalent bond directions  $x$ ,  $y$  and  $z$ . The  $A$  ( $B$ ) sublattice consists of the white (black) sites. Panel (b) is a schematic sketch of the model: Conduction electrons move on the gray, lower graphene layer and interact with the spins sitting on the sites of the top, colored Kitaev layer. The different colors represent the Ising interaction directions, which are the bond directions as in (a).

The dynamics of the spins are described by the isotropic  $K^\alpha = K$  Kitaev model eq. 3.1. The spins of the conduction electrons interact with the Kitaev spins via a Kondo interaction eq. 3.7. The total Hamiltonian is  $H = H_K + H_t + H_J$  with

$$H_t = -t \sum_{\langle i,j \rangle, \sigma} (c_{i,\sigma}^\dagger c_{j,\sigma} + h.c.) \quad (3.6)$$

$$H_J = \frac{J}{2} \sum_{i,\sigma,\sigma',\alpha} c_{i,\sigma}^\dagger \tau_{\sigma,\sigma'}^\alpha c_{i,\sigma'} S_i^\alpha. \quad (3.7)$$

Note that we have assumed for simplicity that graphene and the Kitaev lattice have the same lattice constant. It is fixed to  $a = 246$  pm by assuming that the distance between two lattice points is given by the bond length of graphene [35]. In the real heterostructure the lattices are incommensurate. The effect of this will be discussed later .

### 3.4.2 Majorana Representation

QSLs are usually studied by representing the spin operators in terms of a parton description with slave fermions or also called Abrikosov fermions  $f_{i,\sigma}$

$$S_i^\alpha = \frac{1}{2} \sum_{\sigma,\sigma'} f_{i,\sigma}^\dagger \tau_{\sigma,\sigma'}^\alpha f_{i,\sigma'}, \quad (3.8)$$

### 3.4 From the Kitaev–Kondo Model to an Effective Low Energy Hamiltonian

together with a local single occupancy constraint  $\sum_{\sigma} f_{i,\sigma}^{\dagger} f_{i,\sigma} = 1$ .

Since the Kitaev model can be solved exactly by introducing Majorana fermions  $\chi_i^{\mu}$  with  $\{\chi_i^{\mu}, \chi_j^{\nu}\} = \delta_{\mu,\nu} \delta_{i,j}$ , one seeks for a Majorana description of the Hamiltonians. This can be reached by decomposing the Abrikosov fermions into real Majorana fermions

$$\begin{aligned} f_{i,\uparrow} &= (\chi_i^0 + i\chi_i^3)/\sqrt{2} \\ f_{i,\downarrow} &= (i\chi_i^1 - \chi_i^2)/\sqrt{2} \end{aligned} \quad (3.9)$$

which results, using the single occupancy constraint, into Kitaev’s representation of spins

$$S_i^{\alpha} = i\chi_i^0 \chi_i^{\alpha}. \quad (3.10)$$

In order to get a complete Majorana description of the model, we also decompose the conduction electrons  $c_{i,\sigma}$  into Majorana fermions  $\eta_i^{\mu}$  analogously.

Applying this simple transformation to the Hamiltonian eq. [3.1](#), eq. [3.6](#) and eq. [3.7](#), as it is done in ref. [36](#), yields

$$H_K = \frac{K}{16} \sum_{\langle i,j \rangle_{\alpha}} \chi_i^{\text{T}} M^{\alpha} \chi_i \chi_j^{\text{T}} M^{\alpha} \chi_j \quad (3.11)$$

$$H_t = -t \sum_{\langle i,j \rangle} i\eta_i^{\text{T}} \eta_j \quad (3.12)$$

$$H_J = -\frac{J}{8} \sum_{i,\alpha} \chi_i^{\text{T}} M^{\alpha} \chi_i \eta_i^{\text{T}} M^{\alpha} \eta_i. \quad (3.13)$$

Here  $M$  denotes the spin matrices which are given by

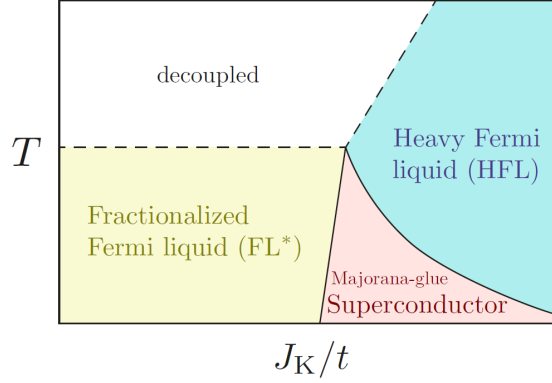
$$M^1 = \tau^3 \otimes i\tau^2, \quad M^2 = i\tau^2 \otimes \tau^0, \quad M^3 = \tau^1 \otimes i\tau^2 \quad (3.14)$$

Note that in order to get eq. [3.12](#) a phase factor  $i$  on the  $B$ -sublattice is introduced with which the notation  $i \in A$  and  $j \in B$  for all sums over  $\langle i, j \rangle$  is adopted.

#### 3.4.3 Parton Mean-Field Theory

Majorana mean-field treatments of the Kitaev model often work well, since ground state properties of the pure Kitaev model are reproduced exactly [37](#). Following earlier work [36](#), we introduce the real mean-field parameters

$$U_{ij}^{\mu\nu} = \langle i\chi_i^{\mu} \chi_j^{\nu} \rangle \quad \text{and} \quad W_i^{\mu\nu} = \langle i\chi_i^{\mu} \eta_i^{\nu} \rangle. \quad (3.15)$$



[Reprinted figure with permission from [U. F. P. Seifert, T. Meng, M. Vojta, Phys. Rev. B., 97, 085118 2018.] Copyright 2021 by the American Physical Society.]

FIGURE 3.2: Schematic phase diagram for the Kitaev–Kondo model in which temperature is plotted against the Kondo coupling  $J_K \equiv J$ . Solid lines are symmetry-breaking phase transitions, while dashed lines denote crossovers.

Neglecting all terms of  $\mathcal{O}\left((i\chi_i^\mu \chi_j^\nu - U_{ij}^{\mu\nu})^2\right)$  and  $\mathcal{O}\left((i\chi_i^\mu \eta_j^\nu - W_{ij}^{\mu\nu})^2\right)$  the mean-field Hamiltonians read

$$H_K = \frac{K}{4} \sum_{\langle i,j \rangle_\alpha} \left( -i\chi_i^\top M^\alpha U_{ij} M^\alpha \chi_j + \frac{1}{2} \text{tr} M^\alpha U_{ij} M^\alpha U_{ij}^\top \right) \quad (3.16)$$

$$H_J = \frac{J}{2} \sum_{i,\alpha} \left( i\chi_i^\top M^\alpha W_i M^\alpha \eta_i - \frac{1}{2} \text{tr} M^\alpha W_i M^\alpha W_i^\top \right). \quad (3.17)$$

The mean-field parameters are assumed to be uniform<sup>2</sup> but dependent on the bond direction. They are determined self consistently by minimizing the energy of the mean-field dependent ground state of the Hamiltonian, consisting of eq. 3.16, eq. 3.17 and eq. 3.12.

Seifert, Meng and Vojta solved the mean-field equations and found at least four distinct phases, see fig. 3.2. The model exhibits exotic and interesting phases. Our focus will be on the heavy Fermi liquid (hFL) phase motivated by the experimental observations. In the hFL phase the mean-field parameters are reduced to  $U = u\mathbb{1}$  and  $W = w\mathbb{1}$  [36].

<sup>2</sup>For  $U_{ij}$  the convention  $i \in A$  and  $j \in B$  is crucial here.

### 3.4.4 Back Transformation to Complex Fermions

The main goal of the following section will be to derive an effective Hamiltonian for the hFL phase in terms of complex fermions rather than Majorana fermions. In the following we will omit all total shifts in the energy (i.e. drop trace terms in eq. 3.16 and eq. 3.17), since our interest is on the relative band structures rather than on the absolute ground state energy. Therefore we can simply include the mean-field parameters  $u$  and  $w$  in the coupling constants by renormalizing the Kitaev and the Kondo coupling  $uK \rightarrow K$  and  $wJ \rightarrow J$ . The simple form of the mean-fields simplifies the Hamiltonian significantly

$$H = - \sum_{\langle i,j \rangle} \left( \frac{K}{4} i\chi_i^T \chi_j + ti\eta_i^T \eta_j \right) + \sum_i \frac{J}{2} i\chi_i^T \eta_i \quad (3.18)$$

where a total shift in the energy has been omitted as mentioned above.

Since it is usually more intuitive to think about matter in terms of spinful, charged complex fermions than in terms of real Majorana fermions, we seek for a description of the hFL phase in terms of Abrikosov fermions  $f_{k,\sigma}$  and conduction electrons  $c_{k,\sigma}$  in momentum space. After transforming back using eq. 3.9 and its analogous form for  $\eta_i^\mu$  only particle number conserving terms are left

$$H = - \sum_{\langle i,j \rangle, \sigma} \left( \frac{K}{4} i f_{i,\sigma}^\dagger f_{j,\sigma} + t i c_{i,\sigma}^\dagger c_{j,\sigma} + h.c. \right) + \frac{J}{2} \sum_{i,\sigma} \left( i f_{i,\sigma}^\dagger c_{i,\sigma} + h.c. \right) + W \sum_{i,\sigma} c_{i,\sigma}^\dagger c_{i,\sigma}. \quad (3.19)$$

The last term constitutes chemical potential  $-W$  for the conduction electrons, which is added to control the filling of electrons in the graphene layer separately.

The Hamiltonian is already diagonal in spin and it will become diagonal in momentum space by Fourier transformation. The indices  $i$  and  $j$  refer to the honeycomb lattice which is not a Bravais lattice and therefore suffers of discrete translational invariance. The honeycomb lattice is split in two hexagonal sublattices  $A$  and  $B$  by setting  $i = (\mathbf{s}, \lambda)$  where  $\mathbf{s}$  refers to the position of the unit cell on sublattice  $A$  and  $\lambda$  to the sublattice (compare to fig. 3.1 (a)). Now momentum is a good quantum number and we can introduce momentum space operators

$$\begin{aligned} c_{\mathbf{k},\lambda,\sigma} &= \frac{1}{\sqrt{N}} \sum_{\mathbf{s}} e^{-i\mathbf{k}\mathbf{r}_{\mathbf{s}}} c_{\mathbf{s},\lambda,\sigma} \\ f_{\mathbf{k},\lambda,\sigma} &= \frac{1}{\sqrt{N}} \sum_{\mathbf{s}} e^{-i\mathbf{k}\mathbf{r}_{\mathbf{s}}} f_{\mathbf{s},\lambda,\sigma} \end{aligned} \quad (3.20)$$

with the total number of unit cells  $N$  and the position in real space  $\mathbf{r}_{\mathbf{s}} = s_1 \mathbf{n}_1 + s_2 \mathbf{n}_2$ .

After performing the Fourier transformation and some gauge transformations the

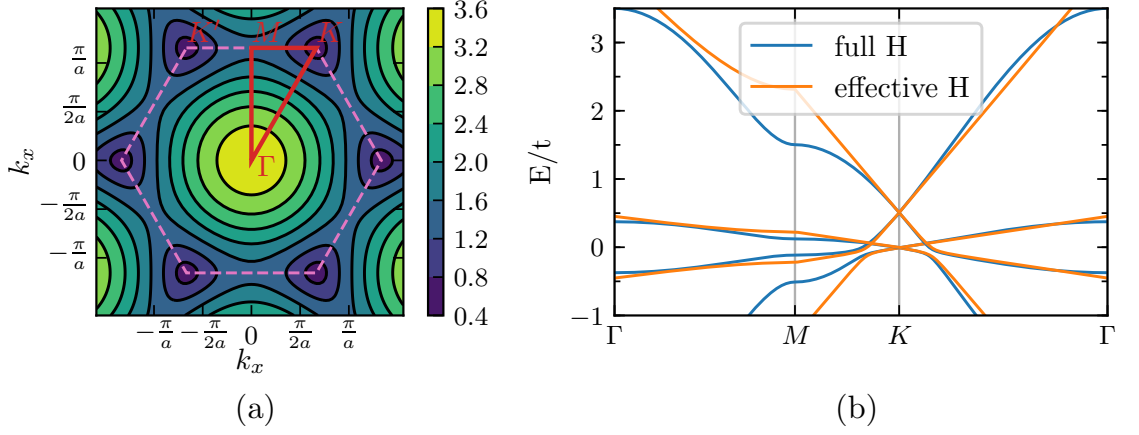


FIGURE 3.3: Panel (a) shows the energy  $E/t$  of the highest band of the non-linear Hamiltonian eq. 3.21 the border of the Brillouin zone (pink, dashed) and a path  $\Gamma M K \Gamma$  (red) along high symmetric lines. In (b) the energies  $E/t$  of all four bands of the non-linear Hamiltonian eq. 3.21 and the effective Hamiltonian eq. 3.25 are plotted.

Hamiltonian reads

$$H = \sum_{\mathbf{k}, \sigma} \begin{pmatrix} c_{k,A,\sigma} \\ c_{k,B,\sigma} \\ f_{k,A,\sigma} \\ f_{k,B,\sigma} \end{pmatrix}^\dagger \begin{pmatrix} W & t\theta_{\mathbf{k}} & \frac{J}{2} & 0 \\ t\theta_{\mathbf{k}}^* & W & 0 & \frac{J}{2} \\ \frac{J}{2} & 0 & 0 & \frac{K}{4}\theta_{\mathbf{k}} \\ 0 & \frac{J}{2} & \frac{K}{4}\theta_{\mathbf{k}}^* & 0 \end{pmatrix} \begin{pmatrix} c_{k,A,\sigma} \\ c_{k,B,\sigma} \\ f_{k,A,\sigma} \\ f_{k,B,\sigma} \end{pmatrix} \quad (3.21)$$

where  $\theta_{\mathbf{k}} = 1 + e^{-i\mathbf{k}n_1} + e^{-i\mathbf{k}n_2}$  is the typical factor appearing in graphene and the Kitaev model.

Even though determining the eigenvalues of the Hamiltonian in eq. 3.21 analytically is in principle possible, the benefit is rather small because of the length of the formulas for general quartic equations. Instead a numerical result for the band structure is plotted in fig. 3.3. Every band is two-fold degenerate due to spin. The characteristic energy spectrum consists of twice a graphene like dispersion relation relatively shifted by  $W$ . The bandwidth of the graphene (Kitaev) bands is set by  $t$  ( $K$ ). Most importantly these two parameters imply two different sized Dirac cones. Since usually  $K \ll t$  the Kitaev bands, located around the Fermi energy, are rather flat, indicating that the quasiparticles' effective masses become indeed large as expected for a hFL. The Kondo coupling parameter  $J$  appears as an effective hybridization between the lower Kitaev and the lower graphene band. Note that a sign change of  $K$  leads to a hybridization of different bands.

### 3.4.5 Effective Low Energy Model

We work with the Hamiltonian from eq. [3.21](#) at fillings around  $\mu = 0$ . In this limit only quasiparticles with a momentum close to the Dirac points  $K$  and  $K'$  are excited, see fig. [3.3](#). The Fermi surface, where quasiparticles are excited, is always close to the  $K$  or the  $K'$ -point. This justifies splitting the Hamiltonian into two parts  $H^K + H^{K'}$  where  $H^K$  ( $H^{K'}$ ) is only non-zero if  $\mathbf{k}$  is closer to  $\zeta = K$  ( $K'$ ) than to  $\zeta = K'$  ( $K$ ). In this thesis the momentum deviation to the Dirac point is denoted by  $\mathbf{q}$ .  $\zeta$  is known as valley degree of freedom and  $H^\zeta$  captures the physics around the relevant Dirac point  $\zeta$ , as seen by the linear expansion of  $\theta_{\mathbf{k}}$  around the Dirac points

$$\theta_{\mathbf{q}+K} = \frac{\sqrt{3}}{2}a(q_x + iq_y) + \mathcal{O}((a|\mathbf{q}|)^2) \quad (3.22)$$

$$\theta_{\mathbf{q}+K'} = \frac{\sqrt{3}}{2}a(-q_x + iq_y) + \mathcal{O}((a|\mathbf{q}|)^2). \quad (3.23)$$

The following calculation will be only done for  $\zeta = K$ , but holds true analogously for  $K'$ . We introduce new operators  $c_{\mathbf{q},\lambda,\sigma}^K = c_{K+\mathbf{q},\lambda,\sigma}$ ,  $f_{\mathbf{q},\lambda,\sigma}^K = f_{K+\mathbf{q},\lambda,\sigma}$  and the spinor

$$\Psi_{\mathbf{q},\sigma}^K = (c_{q,A,\sigma}^K \quad c_{q,B,\sigma}^K \quad f_{q,A,\sigma}^K \quad f_{q,B,\sigma}^K)^T. \quad (3.24)$$

The definition  $\boldsymbol{\tau} = (\tau_x, \tau_y)$  provides further simplifications such that the effective low energy Hamiltonian reads

$$H^K = \sum_{\mathbf{q},\sigma} \Psi_{\mathbf{q},\sigma}^{K\dagger} \begin{pmatrix} W\mathbb{1} + \frac{\sqrt{3}}{2}ta\boldsymbol{\tau}^*\mathbf{q} & \frac{J}{2}\mathbb{1} \\ \frac{J}{2}\mathbb{1} & \frac{\sqrt{3}}{8}Ka\boldsymbol{\tau}^*\mathbf{q} \end{pmatrix} \Psi_{\mathbf{q},\sigma}^K. \quad (3.25)$$

Note that the two-dimensional right-handed Weyl equation appears on the diagonal entries. The other Dirac point  $K'$  contributes Weyl fermions of opposite chirality, such that in total excitations for  $J = 0$  are described by the two-dimensional Dirac equation.

The band structures of the effective Hamiltonian eq. [3.25](#) and the non-linear Hamiltonian eq. [3.21](#) are, close to the Fermi energy, nearly identical as expected, see fig. [3.3](#) (b). In fact the effective Hamiltonian eq. [3.25](#) is an even better description for the band structure of the  $\alpha$ -RuCl<sub>3</sub>-graphene heterostructure.<sup>3</sup> Fig. [3.4](#) compares the band structure of the effective low energy Hamiltonian with the band structure of the  $\alpha$ -RuCl<sub>3</sub>-graphene heterostructure obtained from DFT in ref. [17](#).

The most prominent part of the band structure is the large graphene Dirac cone. The slope of the Dirac cone is adapted by fixing the hopping parameter  $t = 2.6$  eV such that it matches with the DFT data. This is in principle also possible for the Kitaev coupling

<sup>3</sup>The DFT band structure of  $\alpha$ -RuCl<sub>3</sub>-graphene heterostructure shows over a large region linear behavior; further than the band structure of the effective Hamiltonian predicts. Hence, the linear low energy Hamiltonian constitutes a better description in the regions around the Dirac points.

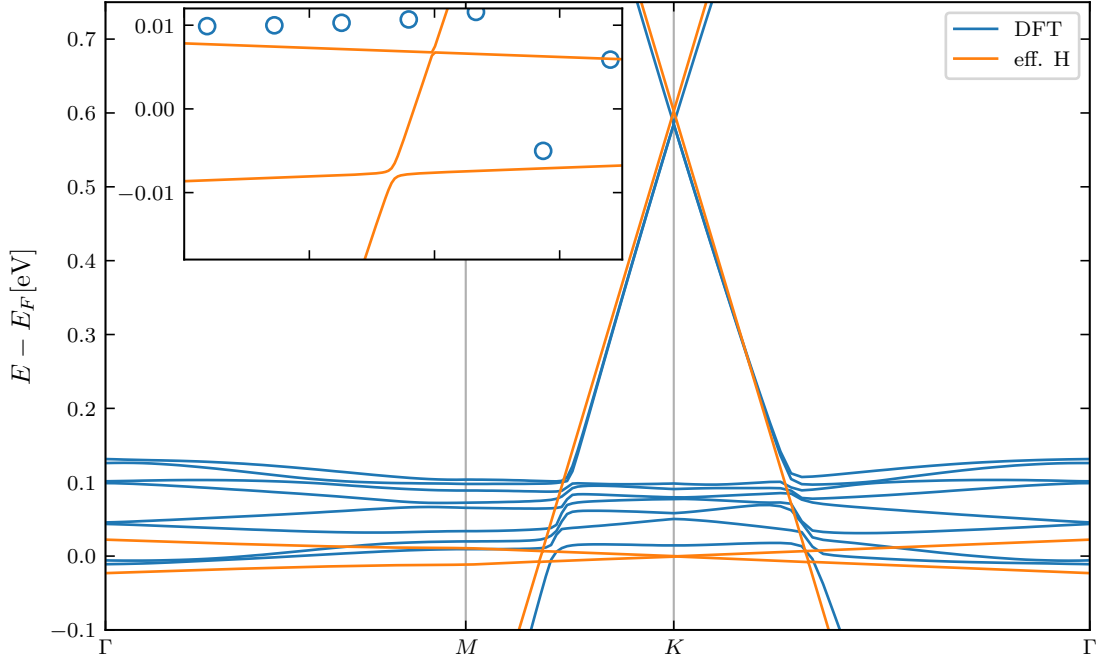


FIGURE 3.4: Band structure of the  $\alpha$ -RuCl<sub>3</sub>-graphene heterostructure obtained via DFT and the effective low energy Hamiltonian eq. 3.25 with  $t = 2.6$  eV and  $K = 25$  meV are adapted such that the effective Hamiltonian describes nicely the DFT band structure while  $W$ ,  $J$  and  $\mu$  are taken from the fit of fig. 3.8. The inset shows a zoom-in to the hybridization region and the DFT data points are the open circles.

$K \approx 25$  meV but due to the plethora of flat bands, resulting from the large unit cell in the *ab-initio* calculations, rather inaccurate. However for the following calculations the precise value of  $K$  is not important, as long as  $K$  is much smaller than  $t$ . The energy shift  $W \approx 0.6$  meV between the graphene Dirac cone and the Kitaev Dirac cone is the result of a charge flow in the heterostructure, causing a surplus of holes (electrons) in the graphene ( $\alpha$ -RuCl<sub>3</sub>) layer [17, 38]. Furthermore the Kitaev Dirac cones of the DFT data are gapped due to a lattice mismatch between graphene and  $\alpha$ -RuCl<sub>3</sub>. In principle such a gap can be easily modelled by a sublattice symmetry breaking term for the Kitaev layer  $\sum_{\lambda, \lambda'} f_{k, \lambda, \sigma}^\dagger \tau_{\lambda, \lambda'}^z f_{k, \lambda', \sigma}$ , but it does not affect the main results of this work, as discussed in the appendix B.1

## 3.5 Landau Level Structure and Quantum Oscillations

### 3.5.1 Magnetic Field and Landau Levels

In the following section the effective model lying in the  $x$ - $y$ -plane is exposed to a magnetic field  $\mathbf{B} = B\hat{e}_z$ . After the application of the quantization rules eq. [2.4](#) on the effective Hamiltonian eq. [3.25](#), it reads<sup>[4](#)</sup>

$$H^K = \sum_{\sigma, q_x} \int dy \Psi_{q_x, \sigma}^K(y)^\dagger \begin{pmatrix} W & \omega_t \hat{a} & \frac{J}{2} & 0 \\ \omega_t \hat{a}^\dagger & W & 0 & \frac{J}{2} \\ \frac{J}{2} & 0 & 0 & \omega_K \hat{a} \\ 0 & \frac{J}{2} & \omega_K \hat{a}^\dagger & 0 \end{pmatrix} \Psi_{q_x, \sigma}^K(y) \quad (3.26)$$

where we have introduced the cyclotron frequencies for graphene  $\omega_t = \frac{\sqrt{3}ta}{\sqrt{2}\ell_B}$  and for the Kitaev model  $\omega_K = \frac{\sqrt{3}Ka}{4\sqrt{2}\ell_B}$ . Note that the cyclotron frequencies for linear band structures are inherently different to those from quadratic band structures, i.e. a Fermi liquid. They are around two orders of magnitude larger and  $\propto \sqrt{B}$ . For the  $\alpha$ -RuCl<sub>3</sub>-graphene heterostructure  $\omega_t = 30.527 \text{ meV} \sqrt{B [\text{T}]}$  while  $\omega_K$  is with roughly  $50 \mu\text{eV} \sqrt{B [\text{T}]}$  by far the smallest energy scale in our model.

To diagonalize eq. [3.26](#) in the LL basis, we need to find a transformation in order to turn the operator-valued entries into complex numbers. This motivates the following transformation

$$\Psi_{q_x, \sigma}^K(y) = \begin{pmatrix} 0 \\ (\Psi_{0, q_x, \sigma}^K)^1 \psi_0(y - y_0) \\ 0 \\ (\Psi_{0, q_x, \sigma}^K)^3 \psi_0(y - y_0) \end{pmatrix} + \sum_{l=1}^{\infty} \begin{pmatrix} (\Psi_{l, q_x, \sigma}^K)^0 \psi_{l-1}(y - y_0) \\ (\Psi_{l, q_x, \sigma}^K)^1 \psi_l(y - y_0) \\ (\Psi_{l, q_x, \sigma}^K)^2 \psi_{l-1}(y - y_0) \\ (\Psi_{l, q_x, \sigma}^K)^3 \psi_l(y - y_0) \end{pmatrix} \quad (3.27)$$

which implicitly defines  $\Psi_{l, q_x, \sigma}$ <sup>[5](#)</sup>. As introduced in sec. [2.3](#),  $\psi_l$  are the eigenfunctions of the harmonic oscillator. Using the transformation together with the orthogonality

<sup>4</sup>Formally we have to transform to continuous space first and then transform  $q_x$  back to a discrete quantum number.

<sup>5</sup>The explicit formula can be obtained by using the orthogonality relations similar as in sec. [2.3](#)

relation of the eigenfunctions we obtain

$$\begin{aligned}
 H^K = & \sum_{q_x, \sigma} \Psi_{0, q_x, \sigma}^{K\dagger} \begin{pmatrix} 0 & 0 & 0 & 0 \\ 0 & W & 0 & \frac{J}{2} \\ 0 & 0 & 0 & 0 \\ 0 & \frac{J}{2} & 0 & 0 \end{pmatrix} \Psi_{0, q_x, \sigma}^K \\
 & + \sum_{l=1, q_x, \sigma} \Psi_{l, q_x, \sigma}^{K\dagger} \begin{pmatrix} W & \omega_t \sqrt{l} & \frac{J}{2} & 0 \\ \omega_t \sqrt{l} & W & 0 & \frac{J}{2} \\ \frac{J}{2} & 0 & 0 & \omega_K \sqrt{l} \\ 0 & \frac{J}{2} & \omega_K \sqrt{l} & 0 \end{pmatrix} \Psi_{l, q_x, \sigma}^K. \quad (3.28)
 \end{aligned}$$

Similar considerations lead to

$$\begin{aligned}
 H^{K'} = & \sum_{q_x, \sigma} \Psi_{0, q_x, \sigma}^{K'\dagger} \begin{pmatrix} W & 0 & \frac{J}{2} & 0 \\ 0 & 0 & 0 & 0 \\ \frac{J}{2} & 0 & 0 & 0 \\ 0 & 0 & 0 & 0 \end{pmatrix} \Psi_{0, q_x, \sigma}^{K'} \\
 & + \sum_{l=1, q_x, \sigma} \Psi_{l, q_x, \sigma}^{K'\dagger} \begin{pmatrix} W & -\omega_t \sqrt{l} & \frac{J}{2} & 0 \\ -\omega_t \sqrt{l} & W & 0 & \frac{J}{2} \\ \frac{J}{2} & 0 & 0 & -\omega_K \sqrt{l} \\ 0 & \frac{J}{2} & -\omega_K \sqrt{l} & 0 \end{pmatrix} \Psi_{l, q_x, \sigma}^{K'} \quad (3.29)
 \end{aligned}$$

which is, ignoring the zeroth LLs, equivalent to eq. [3.28](#). From here on we will ignore the zeroth LLs, since they are inherently different to all other LLs, but irrelevant<sup>6</sup> for the quantum oscillations. Thus the LL Hamiltonian is

$$H_{LL} = \sum_{l=1, q_x, \sigma, \zeta} \Psi_{l, q_x, \sigma}^{\zeta\dagger} \begin{pmatrix} W & \omega_t \sqrt{l} & \frac{J}{2} & 0 \\ \omega_t \sqrt{l} & W & 0 & \frac{J}{2} \\ \frac{J}{2} & 0 & 0 & \omega_K \sqrt{l} \\ 0 & \frac{J}{2} & \omega_K \sqrt{l} & 0 \end{pmatrix} \Psi_{l, q_x, \sigma}^{\zeta}. \quad (3.30)$$

Remarkably the eigenvalues of the Hamiltonian in eq. [3.30](#) can be written down exactly in a compact manner, even though the structure is very similar to the one of the effective

---

<sup>6</sup>The relevant LLs are those which change occupation when the  $B$ -field is tuned. This ultra quantum case where only the zeroth LL is occupied, is not reached in most QOs experiments.

### 3.5 Landau Level Structure and Quantum Oscillations

Hamiltonian eq. [3.21](#). The LLs have energies

$$\begin{aligned}
E_l^0 &= \frac{1}{2} \left( W - (\omega_t + \omega_K) \sqrt{l} - \sqrt{\left( W - (\omega_t - \omega_K) \sqrt{l} \right)^2 + J^2} \right) \\
E_l^1 &= \frac{1}{2} \left( W + (\omega_t + \omega_K) \sqrt{l} - \sqrt{\left( W + (\omega_t - \omega_K) \sqrt{l} \right)^2 + J^2} \right) \\
E_l^2 &= \frac{1}{2} \left( W - (\omega_t + \omega_K) \sqrt{l} + \sqrt{\left( W - (\omega_t - \omega_K) \sqrt{l} \right)^2 + J^2} \right) \\
E_l^3 &= \frac{1}{2} \left( W + (\omega_t + \omega_K) \sqrt{l} + \sqrt{\left( W + (\omega_t - \omega_K) \sqrt{l} \right)^2 + J^2} \right). \tag{3.31}
\end{aligned}$$

and are  $4N_\Phi$ -fold degenerate due to spin and valley degeneracy. The spectrum of the LL-Hamiltonian is plotted in fig. [B.1](#)

The LLs of the effective low energy Hamiltonian have been determined exactly which is possible since eq. [3.25](#) is linear in momentum. As the next section will show, the analytic form of the LLs can be used to calculate the magnetization and hence determine the dHvA effect analytically.

#### 3.5.2 Poles of the Green's function

In order to find observables that oscillate with respect to the magnetic field the grand canonical potential  $\Omega$  is calculated similarly as in the two-dimensional Fermi liquid in sec. [2.5](#). As we are only interested in oscillating observables, we can focus on the oscillating part of the grand canonical potential  $\Omega \equiv \Omega_{\text{osc.}}$ , discarding non-oscillating parts and use the generalized LK formula eq. [2.20](#). Finding the poles of the finite-temperature Green's function  $G_{\nu,\nu'}(i\omega_n) = \delta_{\nu,\nu'}(i\omega_n - (E_l^\nu - \mu))^{-1}$  results in solving four equations which always have the two solutions

$$\begin{aligned}
l_{\pm,n}^* &= \frac{1}{4\omega_K^2 \omega_t^2} \left( (i\omega_n + \mu)(\omega_K + \omega_t) - W\omega_K \right. \\
&\quad \left. \pm \sqrt{\omega_K \omega_t [J^2 - 4(i\omega_n + \mu)^2 + 4W(i\omega_n + \mu)] + [W\omega_K - (\omega_K + \omega_t)(i\omega_n + \mu)]^2} \right)^2. \tag{3.32}
\end{aligned}$$

To simplify eq. [3.32](#) we make use of the fact that  $\omega_K$  is by far the smallest energy scale and expand the root in powers of  $\omega_K/\omega_t \approx 10^{-3}$ . The result are the two poles

$$l_{+,n}^* = \left( \frac{i\omega_n + \mu}{\omega_K} + \frac{J^2/4}{i\omega_n + \mu} \frac{1}{\omega_t} + \mathcal{O}\left(\frac{\omega_K}{\omega_t}\right) \right)^2 \tag{3.33}$$

$$l_{-,n}^* = \frac{1}{\omega_t^2} \left( \frac{J^2/4}{i\omega_n + \mu} + W - (i\omega_n + \mu) + \mathcal{O}\left(\frac{\omega_K}{\omega_t}\right) \right)^2. \tag{3.34}$$

which in principle lead to two types of QOs. As we will see below, the pole  $l_{+,n}^*$  ( $l_{-,n}^*$ ) can be associated with the Fermi surface generated by the Kitaev (graphene) bands. Our interest will be on the QOs generated by  $l_{-,n}^*$ . This is because the clear existence of the Kitaev Dirac cones seems to be an artifact of the effective low energy model and not an universal feature of the  $\alpha$ -RuCl<sub>3</sub>-graphene heterostructure, as the DFT band structure fig. 3.4 suggests. Therefore the experimentally observed QOs cannot originate from the pole  $l_{+,n}^*$ . Apart from this we will see that only the frequency of the QOs from the graphene bands fit to the experiment and that the contributions of  $l_{+,n}^*$  to the thermodynamic potential are small.

### 3.5.3 The Decoupled Limit

In order to check if the so far obtained results are in accordance with known results and to verify the previous assignments of the poles, the oscillatory part of the grand canonical potential  $\Omega$  is calculated in the limit where the graphene layer and the  $\alpha$ -RuCl<sub>3</sub> layer are decoupled, i.e.  $J \rightarrow 0$ .

First we focus on the pole  $l_{-,n}^*$  eq. 3.34 which simplifies in this limit to

$$l_{-,n}^* = \frac{1}{\omega_t^2} (\tilde{\mu}^2 - \omega_n^2 + 2i\omega_n\tilde{\mu}) \quad (3.35)$$

where  $\tilde{\mu} = \mu - W$  is the chemical potential measured from the origin of the graphene Dirac cone. Inserting eq. 3.35 in the generalized LK formula eq. 2.20 the grand canonical potential reads

$$\Omega_{\text{gr}} = 4N_\phi T \sum_{k=1}^{\infty} \sum_{\omega_n > 0}^{\lfloor \tilde{\mu} \rfloor} \frac{1}{k} \cos \left( \frac{2\pi k (\tilde{\mu}^2 - \omega_n^2)}{\omega_t^2} \right) e^{-4\pi k \frac{\omega_n |\tilde{\mu}|}{\omega_t^2}}. \quad (3.36)$$

Eq. 3.36 is the same expression which has also been found in ref. 39 for pure graphene. It describes in general QOs around Dirac cone-like band structures with a slope  $\propto t$ . Note that when the Dirac cone is sufficiently filled  $\tilde{\mu} \gg T$  the temperature shifts of the frequency can be neglected and the exp factor becomes the LK damping factor.

Secondly we determine the pole  $l_{+,n}^*$  in the decoupled limit

$$l_{+,n}^* = \frac{1}{\omega_K^2} (\mu^2 - \omega_n^2 + 2i\omega_n\mu) \quad (3.37)$$

which is obviously the same as eq. 3.35 with  $\omega_t \rightarrow \omega_K$  and where the chemical potential  $\mu$  is now measured from the Fermi energy or equivalently from the origin of the Kitaev Dirac cone. Hence, the grand canonical potential  $\Omega_+$  reads analogously to the one of graphene eq. 3.37, providing clear evidence that the pole  $l_{+,n}^*$  can be assigned to the Kitaev Dirac cone.

### 3.5 Landau Level Structure and Quantum Oscillations

There is another reason why the QOs originating from  $\Omega_+$  can be ignored in the  $\alpha$ -RuCl<sub>3</sub>-graphene heterostructure: Their amplitude is much smaller than the amplitude of the QOs from  $\Omega_{\text{gr}}$  eq. [3.36](#). For  $\mu \gtrsim \omega_K$  the quotient  $\mu/\omega_K^2$  is large compared to temperature, since  $\omega_K$  is so small. Thus, the amplitude decays rapidly with temperature. If however  $\mu \ll \omega_K$  then the sum over  $n$  is truncated very early such that only a few or none Matsubara frequencies can contribute. In any case the size of  $\Omega_+$  stays small compared to  $\Omega_{\text{gr}}$ . This argumentation holds also true for non-zero  $J$ .

#### 3.5.4 The Limit of the $\alpha$ -RuCl<sub>3</sub>-Graphene Heterostructure

In the  $\alpha$ -RuCl<sub>3</sub>-graphene heterostructure the chemical potential is close to the flat bands, see fig. [3.4](#), and the first term of eq. [3.34](#) is not negligible. This is inherently different to the QOs in the decoupled limit. By introducing

$$\Gamma\left(\frac{\mu}{J}, \frac{\omega_n}{J}\right) = 1 + \left( \left(\frac{2\mu}{J}\right)^2 + \left(\frac{2\omega_n}{J}\right)^2 \right)^{-1} \quad (3.38)$$

and assuming  $\mu, T \ll W$ , the pole  $l_{-,n}^* \equiv l_n^*$  simplifies to

$$l_n^* = \left(\frac{W}{\omega_t}\right)^2 \left(1 - 2\frac{i\omega_n}{W} \Gamma\left(\frac{\mu}{J}, \frac{\omega_n}{J}\right)\right). \quad (3.39)$$

There is one subtlety in this approximation i.e. neglecting the term  $\frac{\mu}{W} \frac{J^2/4}{\mu^2 + \omega_n^2}$  which can become large for  $\mu, \omega_n \ll J$ . Consequently the following calculation is not reliable for very low  $T$  and  $\mu$ . Note that we could have determined eq. [3.39](#) directly by setting  $\omega_K = 0$  in eq. [3.31](#), then eq. [3.39](#) would be the only pole.

We can use eq. [3.39](#) to calculate once more with the generalized LK formula eq. [2.20](#)

$$\Omega = 4N_\phi T \sum_{k=1}^{\infty} \frac{1}{k} \cos\left(2\pi k \left[\frac{W}{\omega_t}\right]^2\right) \sum_{n=0}^{\infty} \exp\left(-4\pi k \frac{\omega_n W}{\omega_t^2} \Gamma\left(\frac{\mu}{J}, \frac{\omega_n}{J}\right)\right) \quad (3.40)$$

From that the out-of-plane magnetization is derived

$$\begin{aligned} M &= -\frac{\partial \Omega}{\partial B_z} \\ &= -\frac{8\pi A}{\phi_0} T \left(\frac{W}{\omega_t}\right)^2 \sum_{k=1}^{\infty} \sin\left(2\pi k \left[\frac{W}{\omega_t}\right]^2\right) \sum_{n=0}^{\infty} e^{-4\pi k \frac{\omega_n W}{\omega_t^2} \Gamma\left(\frac{\mu}{J}, \frac{\omega_n}{J}\right)}. \end{aligned} \quad (3.41)$$

where  $\omega_n \ll W$  is used and the degeneracy eq. [2.11](#) inserted. In the experiment only the amplitude of the first harmonic is measured which reads

$$M = -\frac{8\pi A}{\phi_0} T \left(\frac{W}{\omega_t}\right)^2 \sin\left(2\pi \left[\frac{W}{\omega_t}\right]^2\right) \sum_{n=0}^{\infty} e^{-4\pi \frac{\omega_n W}{\omega_t^2} \Gamma\left(\frac{\mu}{J}, \frac{\omega_n}{J}\right)}. \quad (3.42)$$

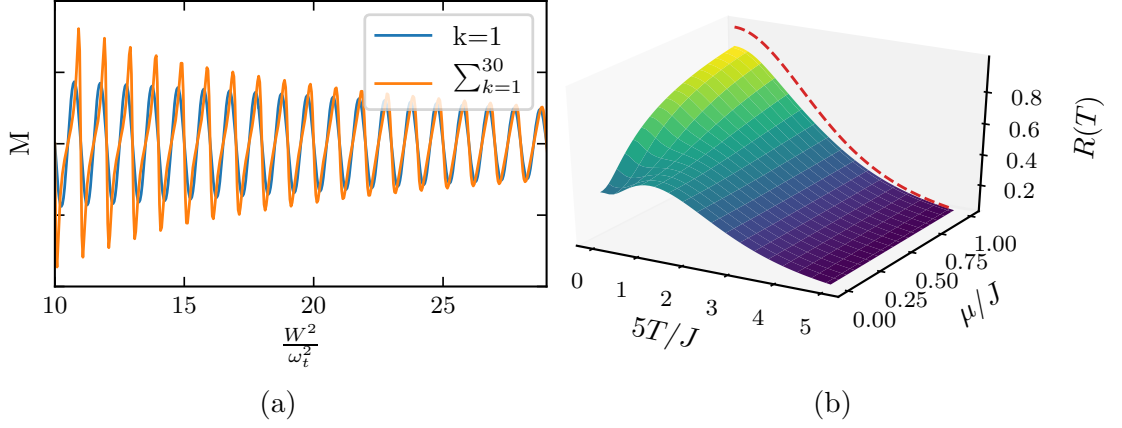


FIGURE 3.5: Panel (a) shows the magnetization, summed over the 30 first harmonics (orange) and only the first harmonic (blue), against  $W^2/\omega_t^2 \propto 1/B$ . In (b) the non-LK behaviour of the QO damping factor  $R(T)$  is plotted as a function of temperature and chemical potential deviation  $\mu/J$ . In the hFL regime for small  $\mu/J$  a characteristic maximum appears around  $T_{\max} \approx J/5$  and at large chemical potential the usual monotonically decreasing LK behavior (red, dashed) is recovered.

In order to analyze the influence of higher harmonics a numerical study has been conducted showing that the summation over  $k$  leads to an asymmetry of the first oscillations, see fig. 3.5 (a). However the experimentally observed oscillations have a higher ratio of  $W^2/\omega_t^2$  where the asymmetry disappears and also the amplitudes coincide, suggesting that a description with the first harmonic is acceptable. Apart from this, the sum over  $n$  is in practice truncated after sufficient convergence.

Remarkably the first harmonic of the magnetization eq. 3.42 can be split into a pure sin-oscillation with frequency  $F = \frac{\hbar}{e} \frac{2W^2}{3t^2 a^2}$  and a damping factor

$$R(T) = 2\chi \sum_{n=0}^{\infty} e^{-2\chi(n+\frac{1}{2})\Gamma(\frac{\mu}{J}, \frac{\omega_n}{J})} \quad \text{with } \chi = 4\pi^2 \frac{TW}{\omega_t^2} \quad (3.43)$$

which constitutes the main result of this thesis. Due to the unusual amplitude of the QOs, they will be referred to as *anomalous QOs*. In accordance with Onsager's prediction eq. 2.1 their frequency  $F = \frac{\hbar}{2\pi e} S$  is given by the area of the Fermi surface  $S = \pi q_F^2$  as if there would be no hybridization.<sup>7</sup> The quantity  $\chi$  takes exactly the form expected in Dirac cone like band structures.

Fig. 3.5 (b) shows the damping factor eq. 3.43 within a parameter regime suitable for the  $\alpha$ -RuCl<sub>3</sub>-graphene heterostructure. Uncommonly the damping factor  $R(T)$  exhibits

<sup>7</sup>The correction  $W \rightarrow W - \mu$  can be derived from eq. 3.34 but will be negligible in the  $\alpha$ -RuCl<sub>3</sub>-graphene heterostructure.

### 3.5 Landau Level Structure and Quantum Oscillations

a maximum at a finite temperature  $T \approx J/5$  for sufficiently small  $\mu$ . The energy scale of the position of the maximum is set by the hybridization energy  $J$ <sup>8</sup>. This remarkable feature distinguishes the damping factor from the monotonous LK damping which is a result of the fact that  $\Gamma \neq 1$  but a function of  $\mu/J$  and  $T/J$ . In the limit of large chemical potential  $\mu \gtrsim J$  the function  $\Gamma(\mu/J, T/J)$  becomes first in good approximation independent of  $n$ ,  $\Gamma(\mu/J, T/J) \rightarrow \Gamma_0(\mu/J)$  and then  $\Gamma_0 \rightarrow 1$ . The damping factor  $R_{\text{LK}}(T)$  then takes the form

$$R_{\text{LK}}(T) = \frac{\chi}{\sinh(\chi)} \quad (3.44)$$

which is the LK damping factor eq. 2.2. Therefore  $\mu$  should be thought of as chemical potential with respect to the effective flat band, determining the distance to the hybridization region. Sufficiently far away from the hybridization region the system behaves in a canonical LK manner.

---

<sup>8</sup>The damping factor  $R$  seems to be very similar to the one found in ref. 10 for free fermions. The main difference is a large factor  $W/\omega_t$  in  $\chi$ . For  $W/\omega_t = 0.5$ , we recover the results from ref. 10. However Knolle and Cooper looked at a two-dimensional electron gas where the scale of the cyclotron frequency is different.

## 3.6 Comparison to the Experimental Data

### 3.6.1 Experimental Samples

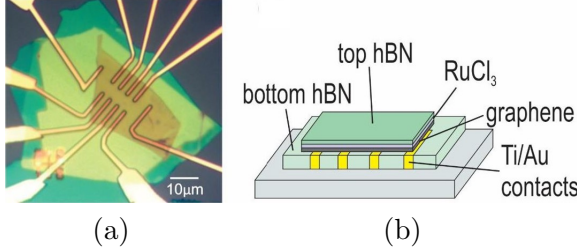


FIGURE 3.6: (a) Optical image of a typical  $\alpha$ - $\text{RuCl}_3$ -graphene device. (b) Schematic illustration of the device, consisting of a flake of hexagonal boron nitride (hBN) as top stacking basis (green), an  $\alpha$ - $\text{RuCl}_3$  nanosheet (purple) and a graphene monolayer (grey). The stack is then transferred onto gold electrodes which are integrated within the bottom hBN flake.

Recently experimentalists have been able to produce and measure samples of  $\alpha$ - $\text{RuCl}_3$ -graphene heterostructures. For details of the complex manufacturing process, see ref. [34]. In the course of developing this theory two additional samples have been produced and measured by Dr. K. Polyudov and Dr. M. Burghard. The results have been published together with the present theory in ref. [1].

All three samples consist of a single layer graphene on a few layers of  $\alpha$ - $\text{RuCl}_3$  of different thickness: sample A from ref. [34] with 20 nm, sample B with 20 nm and sample C with 4 nm both from ref. [1]. As graphene is only expected to directly interact with the

first layers of  $\alpha$ - $\text{RuCl}_3$ , the variation of the thickness should only slightly influence the charge transport through the proximitized graphene. For the devices the longitudinal resistance  $R_{xx}$  in graphene has been measured for magnetic fields from  $\pm 4$  T to  $\pm 12$  T and various temperatures ranging from 1 K up to 20 K.

At this point it should be emphasized that the calculated observable, i.e. the magnetization  $M$ , is different to the observable measured in the experiments. Because of that the dHvA effect is basically compared with the SdH effect. The derivation of the SdH effect/ $R_{xx}$  requires additional assumptions on scattering channels and is more cumbersome than of an observable which is directly derived from the thermodynamic potential. It is unknown if the SdH effect would also be analytically accessible. Moreover it is likely that the magnetization has the same features as the longitudinal resistance, since the frequency and temperature dependence for metallic systems are within the canonical LK theory the same [4]. In summary I believe that there is sufficient evidence to assume that the anomalous damping factor of the magnetization eq. 3.43 allows to understand the main features of the magnetotransport measurements.

### 3.6.2 Fitting

For the fitting procedure the samples' amplitudes for various temperatures at a fixed  $B$ -field are determined.<sup>9</sup> The  $B$ -fields of the amplitudes are chosen such that the signal is strong in order to minimize errors, i.e. at medium to high  $B$ -fields around 11 T and at the extremum of an oscillation. In fig. 3.7 the obtained data points are fitted with the non-LK amplitude  $R(T)$  from eq. 3.43.

The fitting procedure is complex since only few temperatures have been measured experimentally (between 6 and 13 depending on the sample), whereas we would in principle like to fit five parameters from eq. 3.43.<sup>10</sup> While it is possible to produce very good fits, with five (or even only four) free parameters the risk of overfitting the data is very high, becoming evident in the fact that the fitting procedures converge on different results. In order to get more reliable results we make some physical consideration first in order to reduce the number of fitting values.

Already in sec. 3.5.1 we have fixed the value of  $t$  and  $K$  by a comparison to the DFT data and hence found values for the cyclotron frequencies  $\omega_t$  and  $\omega_K$ . Note that the quotient  $\omega_K/\omega_t \approx 10^{-3}$  is small as required in the derivation of the QOs. The value of  $\omega_t$  then depends on the  $B$ -field at which the sample's amplitude was determined.

The frequency spectrum of each sample has a sharp maximum at the oscillation frequency  $F$ . Using the predicted frequency of the magnetic oscillations eq. 3.42 the value of  $W \approx 0.6$  eV (exact values are listed in tab. 3.1) can be inferred for every sample.

By determining  $W$  and  $\omega_t$  separately, only three free parameters are left. In the fitting procedure the parameters now always converged on the same value independently from their initial value, suggesting that the data is not overfitted. From the fits, the chemical potential  $|\mu| < 0.5$  meV and the key parameter the Kondo exchange  $J \approx 2$  meV are extracted for every sample. The detailed values for each sample are given in tab. 3.1.

In order to be able to compare the theory of *anomalous QOs* to the canonical LK theory, the experimental data is also fitted with a rescaled LK damping factor  $R_{\text{LK}}(\chi)$  from eq. 3.44, see the dashed lines in fig. 3.7. Since the values for  $W$  and  $\omega_t$  are already fixed, the only free parameter is the rescaling constant. In fig. B.3 in the appendix there is additionally the cyclotron frequency adjusted. This clearly improves the LK fits but the fitted values for  $\omega_t$  are contradictory to the microscopic values  $\omega_t = \frac{\sqrt{3}ta}{\sqrt{2}l_B}$  which are consistent with the DFT data and the frequency.<sup>11</sup>

For fig. 3.7 only selected amplitudes of each sample have been fitted. However the

<sup>9</sup>Sample A is an exception. The only accessible data was the temperature dependence of the maximum in the Fourier spectrum. This can be treated as the amplitude at a  $B$ -field, corresponding to the mean value of the Fourier window.

<sup>10</sup>The five parameters are  $\mu$ ,  $J$ ,  $W$ ,  $\omega_t$  and a rescaling factor which adapts the experimental data to a regime between 0 and 1.

<sup>11</sup>In this case fitting  $\omega_t$  or  $W$  are equivalent, since only the quotient of the two quantities appears in the LK damping factor. A change of  $W$  is also at odds the DFT data and the frequency.

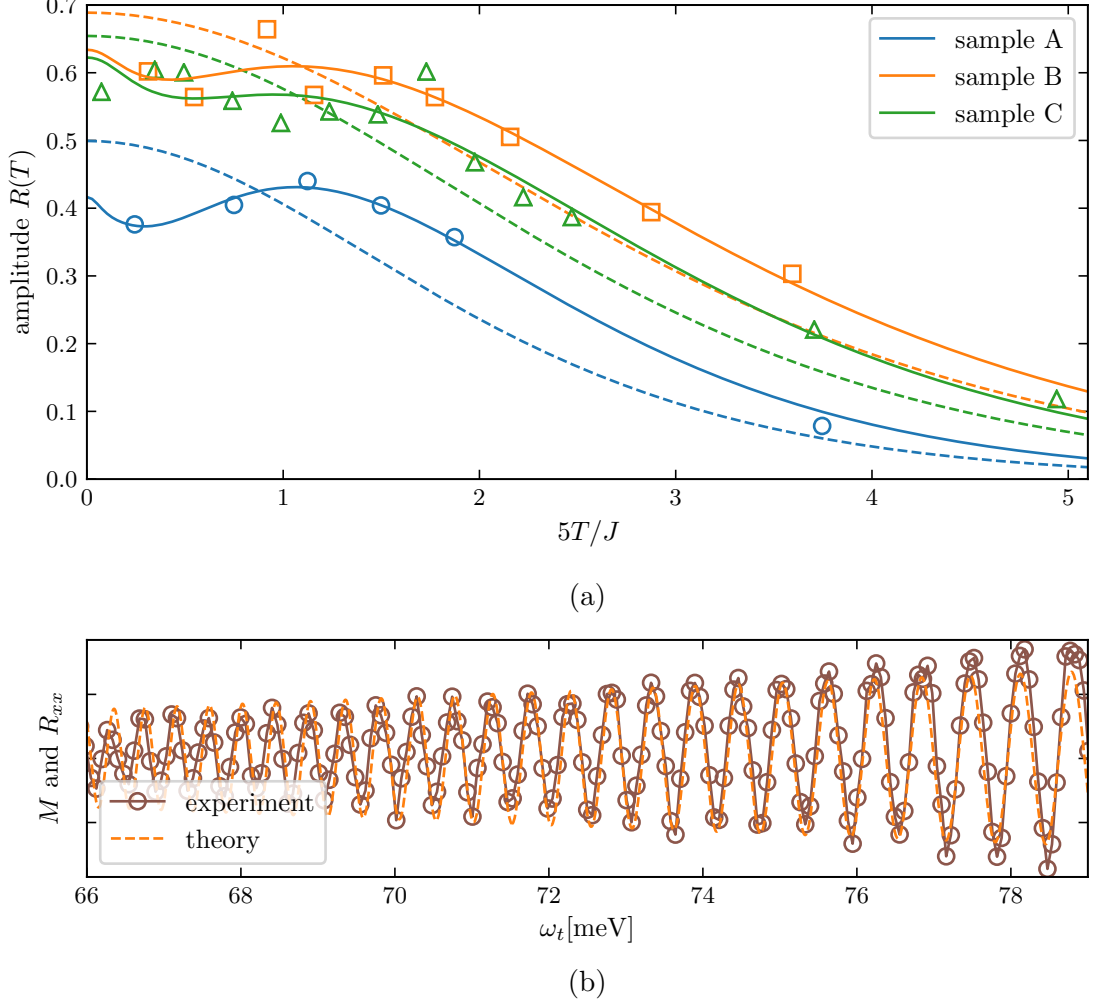


FIGURE 3.7: Panel (a): Fit of the experimental data (open symbols) with the theoretical predicted curves of eq. 3.43 (solid lines) and the rescaled LK damping factor  $R_{LK}$  (dashed lines). Fitting values and quality criteria are given in tab 3.1 and tab. B.1. Panel (b): The experimentally determined longitudinal resistance  $R_{xx}$  of sample B at 3.8K (open circles which are connected by solid lines to guide the eye) and the analytically determined magnetization  $M$  (dashed line) of eq. 3.42 are plotted against the cyclotron frequency of graphene  $\omega_t \propto \sqrt{B}$ . The parameters for  $M$  are taken from the amplitude decay fit in fig. 3.8, with parameters tabulated in tab 3.1.

### 3.6 Comparison to the Experimental Data

sample	A	B	C	B for various $B$ s
$F$	365 T	390 T	386 T	390 T
$B$	10 T	11.7 T	10 T	8/9.5/11/11.7 T
$W$	583 meV	603 meV	600 meV	603 meV
$\omega_t$	96.5 meV	104 meV	96.5 meV	86/94/101/104 meV
$J$	2.30 meV	1.80 meV	1.75 meV	1.70 meV
$ \mu $	271 $\mu$ eV	308 $\mu$ eV	363 $\mu$ eV	407 $\mu$ eV
$R^2$	0.99917	0.99770	0.99505	-
Adj. $R^2$	0.99834	0.99655	0.99357	-

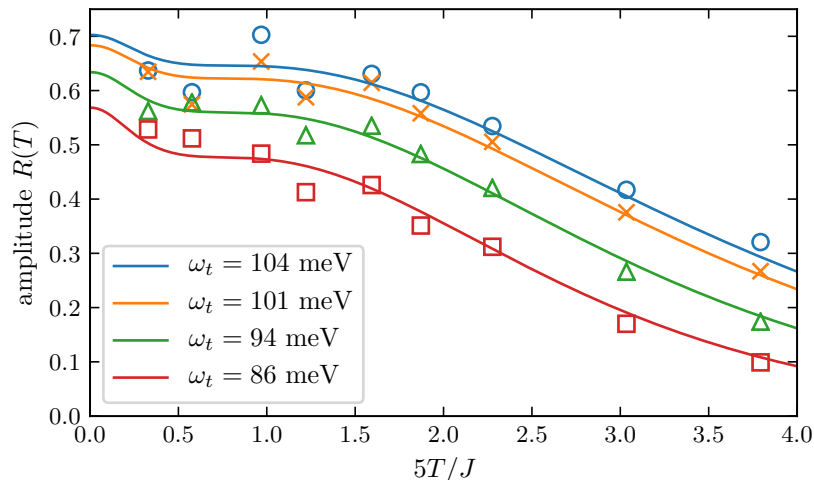
TABLE 3.1: Fitting parameters and quality criteria of the solid curves in fig. 3.7 (first three columns) and fig. 3.8 (last column).  $W$  and  $\omega_t$  are calculated from the magnetic field  $B$  and the frequency  $F$ ,  $J$  and  $\mu$  are fitting parameters. As quality criteria the  $R$ -squared and  $Adjusted R$ -squared measure are shown in the last two rows.

microscopic parameters of the samples should not change if an amplitude at a different magnetic field is chosen. Fig. 3.8 indicates that it is possible to robustly fit multiple amplitudes at the same time. For this fitting procedure  $\omega_t$  is calculated according to the amplitudes'  $B$ -fields while  $\mu$  and  $J$  are optimized for all curves simultaneously.

#### 3.6.3 Discussion of the Fits

The fitting parameters are listed in tab. 3.1 and tab. B.1 for the LK fits. It is evident that for all samples the energy shifts  $W$ , originating from the charge transfer between the two layers, are very similar. All values for  $W$  match remarkably well with the DFT data, see the shift of the origins of the Dirac cones in fig. 3.4. This is expected from the theory, since  $W$  sets the size of the Fermi surface which is robust against sample deviations. Note that the unconventional large size of  $W$  has enabled the possibility to study highly doped graphene, since with standard gating methods the chemical potential in graphene has never been shifted by an energy scale as large as  $W = 0.6$  eV.

The other microscopic parameters  $|\mu| < 0.5$  meV and  $J \approx 2$  meV are small and depend rather on the sample. This is due to the fact that the fabrication process of the samples is complex and only limitedly reproducible, such that deviations of a few hundred  $\mu$ eV can be expected. Moreover, the theory itself predicts a strong sample dependence as the damping factor  $R(T)$  is very sensitive to small changes of  $\mu$  and  $J$ . In comparison to the DFT band structure the value of  $J$  appears to be surprisingly small. The reason for this difference is not known, it could originate from the larger unit cell in the DFT calculations or there may be additional interactions present in the actual heterostructure which introduce gaps between the graphene and Kitaev bands but are irrelevant for the QOs. Finally and most importantly it happens often that DFT fails to produce some microscopic details of the band structure, especially gaps [40, 41].

FIGURE 3.8: Simultaneous fit of various amplitudes of sample B at different  $B$ -fields

The deviations of the experimental data points to the theory curves in fig. 3.7 (a) depend on the sample. The few data points of sample A match nearly perfectly with the theory curve. For the samples B and C more temperatures have been measured. In these measurements deviations to the theory curve occur only at low temperatures. Unfortunately it is not possible to show error bars of the experimental data to evaluate if these deviations are robust and hence meaningful. The samples can only endure a single complete measurement cycle, since the repeated temperature swiping imposes a significant amount of mechanical stress onto them due to the different thermal expansion coefficients of the device materials. If the low temperature deviations are indeed robust properties of the heterostructure, it is most likely that small energy scales such as  $\omega_K$ , which have been effectively set to zero in the derivation, influence the temperature dependence at small temperatures.

In total the theory of *anomalous QOs* shows very good and convincing correspondence with the various measured samples. Even though the curves of the novel theory seem to not completely explain the data, they perform qualitatively and quantitatively significantly better than the standard LK theory fits, see tab. B.1 and tab. 3.1. The LK fits can not reproduce the maximum and the flat decay which is clearly visible in the experimental data. The quality of the fits is evaluated with the in-built *Mathematica* routine *Adjusted R-squared* which takes account of the different number of fitting parameters. *Adjusted R-squared* is in this case a more meaningful quality criterion than the standard *R-squared* measure. Even if  $\omega_t$  is treated as fitting parameter, leading to values which are odds with the microscopic values derived from DFT, the anomalous amplitude  $R(T)$  gives quantitatively the better fit.

In order to clear remaining doubts that too many parameters are extracted from too

few data points, fig. 3.8 is shown. By effectively tripling the number of data points while reproducing roughly the fitting parameters, the reliability of the single amplitude fits is underlined.

### 3.6.4 Exponential Suppression of the QOs within the Hybridization Region

In general the total amplitude of *anomalous QOs* is suppressed exponentially in the quotient  $\Delta/\omega_c$  of gap or hybridization size  $\Delta$  over cyclotron energy  $\omega_c$ , so that the QOs are only observable at very high  $B$ -fields and very small gaps [10]. Here we will explore the total amplitude behavior of the *anomalous QOs* in the  $\alpha$ -RuCl<sub>3</sub>-graphene heterostructure.

The maximum  $R_{\max}$  of  $R(T)$  from eq. 3.43 is roughly located at  $T_{\max} \approx J/5$ . The decay of  $R_{\max} = R(J/5)$  is dominated by the zeroth Matsubara frequency, since all other terms of the sum lead to a stronger decay. As a result we find that  $R(J/5)$  is damped exponentially with the size of the hybridization region  $J$

$$R_{\max} \propto \exp\left(-\kappa \frac{JW}{\omega_t^2}\right) \quad (3.45)$$

where  $\kappa$  is a constant of order 1. This predicts that the QOs should only be observable up to a hybridization energy scale  $J_{\max} \sim \omega_t^2/W$ . For the  $\alpha$ -RuCl<sub>3</sub>-graphene heterostructure  $J_{\max}$  is approximately  $1.6 \text{ meV} \times B [\text{T}]$  which is already for small magnetic fields sufficiently higher than the predicted values of  $J \approx 2 \text{ meV}$ . Hence, the exponent remains small for the applied  $B$ -fields of 4 T to 12 T. Therefore the total amplitude in the  $\alpha$ -RuCl<sub>3</sub>-graphene heterostructure is not exponentially small making the QOs experimentally observable.

## 3.7 Discussion

The presented theory of *anomalous QOs* is based on an effective low energy description of the hFL phase of the Kitaev-Kondo model. Its energy spectrum describes the electronic structure of  $\alpha$ -RuCl<sub>3</sub>-graphene heterostructures. The most striking feature in this theory is that it is able to explain the experimentally measured, non-LK damping factor showing a characteristic maximum at finite temperature. In previous work [34] the maximum has been interpreted as a signature of the transition to long-range magnetic order in  $\alpha$ -RuCl<sub>3</sub> because it roughly coincides with the material's Néel temperature. It has been argued that due to the antiferromagnetic ordering, spin scattering effects are enhanced which leads to an upturn of the resistivity at low temperature. This is however considered to be unlikely since impurity scattering should increase the Dingle temperature and therefore decrease the total amplitude. Note additionally that the magnetic transition has so far not been observed in the heterostructure but only

in bulk  $\alpha$ -RuCl<sub>3</sub>. These arguments put the presented microscopic theory in favor as explanation of the observed maximum of the damping factor at finite temperature.

The observation that the experimental magnetotransport measurements are consistent with the developed theory has interesting consequences. First of all it provides further evidence that the spin dynamics of the  $\alpha$ -RuCl<sub>3</sub> layer in the heterostructure is indeed described by the seminal Kitaev model. The frequency of the QOs measurements confirm the large doping of the graphene layer, initially found in ref. [17, 38]. While usually amplitude measurements only allow to determine the effective mass or equivalently the Fermi velocity, the theory of *anomalous QOs* also allows to infer the extremely small values of  $\mu$  and  $J$ . The possibility to extract the low energy scales of the band structure can be turned into useful tool. Note however that the found values for  $J$  and  $K$  constitute by mean-field renormalized values. To determine their values in the initial model, the values of the mean-fields  $u$  and  $w$  need to be calculated.

Furthermore the results suggest that the character of the fractionalized excitations of the Kitaev model in the heterostructure changes. Formerly, i.e. for  $J = 0$ , these excitations have been charge neutral Majorana fermions lacking a  $U(1)$  symmetry. However in the heterostructure they acquire charge via the Kondo coupling of the Kitaev spins to the itinerant electrons of the graphene layer, which can be measured in form of the *anomalous QOs*.

Although the theory seems to be highly adopted to the  $\alpha$ -RuCl<sub>3</sub>-graphene heterostructure, it is widely applicable to heavy Fermi liquids which are hybridized with a linear, Dirac-like band. Importantly, the observation of *anomalous QO* is not directly connected to the proximate QSL behavior of the  $\alpha$ -RuCl<sub>3</sub> layer, but is a result of an effective flat band at the Fermi energy. The effective flat band appears in the  $\alpha$ -RuCl<sub>3</sub>-graphene heterostructure, because the fractionalized excitations of the Kitaev model are compared to the excitations of graphene, nearly non-dispersive and gapless. The key for an experimental observation of *anomalous QOs* in a hFL is that the parameters of the heterostructure do not lead to an exponential suppression of the total amplitude — a fact which is far more easily fulfilled with linearly dispersive bands than with quadratically dispersive ones.

# Chapter 4

## Conclusion

Nowadays, QO are more than just an experimental technique to determine a metal's Fermi surface. They constitute a possibility to explore novel behavior in strongly correlated quantum materials, like the discussed heterostructure of graphene on a proximate QSL. Deviations to the canonical LK theory provide an opportunity for probing material properties with the venerable method of QO measurements. While the discussion of the semi-classical description of QOs in metals seems to be settled, the field of QOs in insulators has just begun and many questions are left to be answered.

In the appendix [A](#) of this thesis I gave an alternative derivation for the generalized LK formula which is more easily accessible for readers without background in holographic correspondence. The generalized LK formula provides an intuitive understanding of the interplay of the poles of the Green's function and QOs of the thermodynamic potential. By exploiting this relation, I rederived well-known results for the thermodynamic potential and the magnetization in the two-dimensional Fermi liquid in a simple and short manner in chapter [2](#).

In the third chapter, I introduced the  $\alpha$ -RuCl<sub>3</sub>-graphene heterostructure, whose  $\alpha$ -RuCl<sub>3</sub> layer is at least proximate to the sought-after Kitaev QSL. The hFL phase of the Kitaev-Kondo model constitutes an effective description for this heterostructure. The model lets Kitaev spins interact Kondo-like with the itinerant graphene electrons. Following earlier work, I performed a Majorana mean-field theory which lead to an effective low energy Hamiltonian. Interestingly the LLs of this Hamiltonian can be determined analytically and hence also the Green's function. Exploiting again the generalized LK formula, I derived an analytic formula for the magnetization which remarkably features QOs with a non-LK temperature dependence. Within a suitable region close to the effectively flat band this theory of *anomalous QOs* predicts a maximum at a temperature set by the hybridization scale. Even though the theory is developed for the specific example of the  $\alpha$ -RuCl<sub>3</sub>-graphene heterostructure, it is applicable for any hFL hybridized with a Dirac cone-like band structure. Furthermore the derived effective low energy model of the  $\alpha$ -RuCl<sub>3</sub>-graphene heterostructure may be used as a starting point to determine other quantities in the heterostructure which can than be probed in experiments, e.g in ref. [42](#) a microscopic theory for plasmon excitations in  $\alpha$ -RuCl<sub>3</sub>-graphene heterostructures is developed.

## Chapter 4 Conclusion

Finally, I compared the results of the theory of *anomalous QOs* in-depth with recent experimental measurements for three different heterostructure samples. They all show convincing correspondence to the developed theory and improve quantitatively over a description with the standard LK theory. The found results are also in accordance with *ab-initio* calculations. The correspondence of experiment and theory has led to the conclusion that the fractionalized excitations of the the Kitaev model have acquired charge by the effective hybridization of the Kondo interaction. Furthermore these findings can be turned into a versatile tool to extract small energy scales out of the strongly correlated layer.

Although this thesis has shown how non-LK QOs may emerge and what their connection to microscopic parameters is, many questions remain open. The detailed mechanism how the fractionalized excitations have acquired charge is still unsatisfactory answered. Additionally, it is open which alternative scenarios could lead to *anomalous QOs* in correlated insulators. Overall, this thesis has paved the way for understanding non-LK behavior in strongly correlated materials.

## Bibliography

- [1] V. Leeb, K. Polyudov, S. Mashhadi, S. Biswas, R. Valentí, M. Burghard, and J. Knolle, “Anomalous quantum oscillations in a heterostructure of graphene on a proximate quantum spin liquid,” *Phys. Rev. Lett.*, vol. 126, p. 097201, 2021. DOI: [10.1103/PhysRevLett.126.097201](https://doi.org/10.1103/PhysRevLett.126.097201).
- [2] I. Lifshitz and A. Kosevich, “Theory of magnetic susceptibility in metals at low temperatures,” *Sov. Phys. JETP*, vol. 2, no. 4, pp. 636–645, 1956.
- [3] W. J. de Haas and P. M. van Alphen, “The dependence of the susceptibility of diamagnetic metals upon the field,” *Proceedings of the Academy of Science of Amsterdam*, vol. 33, pp. 1106–1118, 1930. [Online]. Available: <https://www.dwc.knaw.nl/DL/publications/PU00015989.pdf>.
- [4] D. Shoenberg, *Magnetic Oscillations in Metals*, ser. Cambridge Monographs on Physics. Cambridge, England: Cambridge University Press, 1984. DOI: [10.1017/CB09780511897870](https://doi.org/10.1017/CB09780511897870).
- [5] N. Hussey, M. Abdel-Jawad, A. Carrington, A. P. Mackenzie, and L. Balicas, “A coherent three-dimensional fermi surface in a high-transition-temperature superconductor,” *Nature*, vol. 425, pp. 814–817, 2003. DOI: [10.1038/nature01981](https://doi.org/10.1038/nature01981).
- [6] B. S. Tan et al., “Unconventional fermi surface in an insulating state,” *Science*, vol. 349, no. 6245, pp. 287–290, 2015. DOI: [10.1126/science.aaa7974](https://doi.org/10.1126/science.aaa7974).
- [7] M. Hartstein et al., “Fermi surface in the absence of a fermi liquid in the kondo insulator SmB<sub>6</sub>,” *Nature Physics*, vol. 14, no. 2, pp. 166–172, 2017. DOI: [10.1038/nphys4295](https://doi.org/10.1038/nphys4295).
- [8] H. Liu et al., “Fermi surfaces in kondo insulators,” *Journal of Physics: Condensed Matter*, vol. 30, no. 16, 16LT01, 2018. DOI: [10.1088/1361-648x/aaa522](https://doi.org/10.1088/1361-648x/aaa522).
- [9] Z. Xiang et al., “Quantum oscillations of electrical resistivity in an insulator,” *Science*, vol. 362, no. 6410, pp. 65–69, 2018. DOI: [10.1126/science.aap9607](https://doi.org/10.1126/science.aap9607).
- [10] J. Knolle and N. R. Cooper, “Quantum oscillations without a fermi surface and the anomalous de haas–van alphen effect,” *Phys. Rev. Lett.*, vol. 115, p. 146401, 2015. DOI: [10.1103/PhysRevLett.115.146401](https://doi.org/10.1103/PhysRevLett.115.146401).
- [11] L. Zhang, X. Song, and F. Wang, “Quantum oscillation in narrow-gap topological insulators,” *Phys. Rev. Lett.*, vol. 116, p. 046404, 4 2016. DOI: [10.1103/PhysRevLett.116.046404](https://doi.org/10.1103/PhysRevLett.116.046404).

## Bibliography

- [12] O. Erten, P. Ghaemi, and P. Coleman, “Kondo breakdown and quantum oscillations in  $\text{SmB}_6$ ,” *Phys. Rev. Lett.*, vol. 116, p. 046 403, 2016. DOI: [10.1103/PhysRevLett.116.046403](https://doi.org/10.1103/PhysRevLett.116.046403).
- [13] H. Shen and L. Fu, “Quantum oscillation from in-gap states and a non-hermitian landau level problem,” *Phys. Rev. Lett.*, vol. 121, p. 026 403, 2018. DOI: [10.1103/PhysRevLett.121.026403](https://doi.org/10.1103/PhysRevLett.121.026403).
- [14] D. Chowdhury, I. Sodemann, and T. Senthil, “Mixed-valence insulators with neutral fermi surfaces,” *Nature Communications*, vol. 9, no. 1, 2018. DOI: [10.1038/s41467-018-04163-2](https://doi.org/10.1038/s41467-018-04163-2).
- [15] I. Sodemann, D. Chowdhury, and T. Senthil, “Quantum oscillations in insulators with neutral fermi surfaces,” *Phys. Rev. B*, vol. 97, p. 045 152, 2018. DOI: [10.1103/PhysRevB.97.045152](https://doi.org/10.1103/PhysRevB.97.045152).
- [16] B. Zhou, J. Balgley, P. Lampen-Kelley, J.-Q. Yan, D. G. Mandrus, and E. A. Henriksen, “Evidence for charge transfer and proximate magnetism in graphene- $\alpha$ - $\text{RuCl}_3$  heterostructures,” *Phys. Rev. B*, vol. 100, p. 165 426, 2019. DOI: [10.1103/PhysRevB.100.165426](https://doi.org/10.1103/PhysRevB.100.165426).
- [17] S. Biswas, Y. Li, S. Winter, J. Knolle, and R. Valentí, “Electronic properties of  $\alpha$ - $\text{RuCl}_3$  in proximity to graphene,” *Phys. Rev. Lett.*, vol. 123, p. 237 201, 2019. DOI: [10.1103/PhysRevLett.123.237201](https://doi.org/10.1103/PhysRevLett.123.237201).
- [18] L. Onsager, “Interpretation of the de haas-van alphen effect,” *The London, Edinburgh, and Dublin Philosophical Magazine and Journal of Science*, vol. 43, no. 344, pp. 1006–1008, 1952. [Online]. Available: <https://www.tandfonline.com/doi/abs/10.1080/14786440908521019>.
- [19] P. D. Grigoriev, “Theory of the shubnikov–de haas effect in quasi-two-dimensional metals,” *Phys. Rev. B*, vol. 67, p. 144 401, 2003. DOI: [10.1103/PhysRevB.67.144401](https://doi.org/10.1103/PhysRevB.67.144401).
- [20] J. Klier, “Magnetotransport in novel dirac systems,” 43.21.02; LK 01, Ph.D. dissertation, Karlsruher Institut für Technologie (KIT), 2019, 187 pp. DOI: [10.5445/IR/1000090851](https://doi.org/10.5445/IR/1000090851).
- [21] P. Coleman, *Introduction to Many-Body Physics*, 3rd ed. Cambridge: Cambridge University Press, 2019.
- [22] J. M. Luttinger and J. C. Ward, “Ground-state energy of a many-fermion system. ii,” *Phys. Rev.*, vol. 118, pp. 1417–1427, 1960. DOI: [10.1103/PhysRev.118.1417](https://doi.org/10.1103/PhysRev.118.1417).
- [23] S. A. Hartnoll and D. M. Hofman, “Generalized lifshitz-kosevich scaling at quantum criticality from the holographic correspondence,” *Physical Review B*, vol. 81, no. 15, 2010. DOI: [10.1103/physrevb.81.155125](https://doi.org/10.1103/physrevb.81.155125).

- [24] P. Anderson, “Resonating valence bonds: A new kind of insulator?” *Materials Research Bulletin*, vol. 8, no. 2, pp. 153–160, 1973. DOI: [https://doi.org/10.1016/0025-5408\(73\)90167-0](https://doi.org/10.1016/0025-5408(73)90167-0).
- [25] J. Knolle and R. Moessner, “A field guide to spin liquids,” *Annual Review of Condensed Matter Physics*, vol. 10, no. 1, pp. 451–472, 2019. DOI: [10.1146/annurev-conmatphys-031218-013401](https://doi.org/10.1146/annurev-conmatphys-031218-013401).
- [26] S. Lucile and L. Balents, “Quantum spin liquids: A review,” *Reports on Progress in Physics*, vol. 80, no. 1, p. 016 502, 2016. DOI: [10.1088/0034-4885/80/1/016502](https://doi.org/10.1088/0034-4885/80/1/016502).
- [27] A. Kitaev, “Fault-tolerant quantum computation by anyons,” *Annals of Physics*, vol. 303, no. 1, pp. 2–30, 2003. DOI: [https://doi.org/10.1016/S0003-4916\(02\)00018-0](https://doi.org/10.1016/S0003-4916(02)00018-0).
- [28] A. Kitaev, “Anyons in an exactly solved model and beyond,” *Annals of Physics*, vol. 321, no. 1, pp. 2–111, 2006. DOI: [10.1016/j.aop.2005.10.005](https://doi.org/10.1016/j.aop.2005.10.005).
- [29] M. Hermanns, I. Kimchi, and J. Knolle, “Physics of the kitaev model: Fractionalization, dynamic correlations, and material connections,” *Annual Review of Condensed Matter Physics*, vol. 9, no. 1, pp. 17–33, 2018. DOI: [10.1146/annurev-conmatphys-033117-053934](https://doi.org/10.1146/annurev-conmatphys-033117-053934).
- [30] S. Mandal and A. M. Jayannavar, *An introduction to kitaev model-i*, 2020. arXiv: [2006.11549](https://arxiv.org/abs/2006.11549).
- [31] E. H. Lieb, “Flux phase of the half-filled band,” *Phys. Rev. Lett.*, vol. 73, pp. 2158–2161, 1994. DOI: [10.1103/PhysRevLett.73.2158](https://doi.org/10.1103/PhysRevLett.73.2158).
- [32] G. Jackeli and G. Khaliullin, “Mott insulators in the strong spin-orbit coupling limit: From heisenberg to a quantum compass and kitaev models,” *Phys. Rev. Lett.*, vol. 102, p. 017 205, 2009. DOI: [10.1103/PhysRevLett.102.017205](https://doi.org/10.1103/PhysRevLett.102.017205).
- [33] R. D. Johnson et al., “Monoclinic crystal structure of  $\alpha$ -RuCl<sub>3</sub> and the zigzag antiferromagnetic ground state,” *Phys. Rev. B*, vol. 92, p. 235 119, 23 2015. DOI: [10.1103/PhysRevB.92.235119](https://doi.org/10.1103/PhysRevB.92.235119).
- [34] S. Mashhadi et al., “Spin-split band hybridization in graphene proximitized with  $\alpha$ -RuCl<sub>3</sub> nanosheets,” *Nano Letters*, vol. 19, no. 7, pp. 4659–4665, 2019. DOI: [10.1021/acs.nanolett.9b01691](https://doi.org/10.1021/acs.nanolett.9b01691).
- [35] A. H. Castro Neto, F. Guinea, N. M. R. Peres, K. S. Novoselov, and A. K. Geim, “The electronic properties of graphene,” *Rev. Mod. Phys.*, vol. 81, pp. 109–162, Jan. 2009. DOI: [10.1103/RevModPhys.81.109](https://doi.org/10.1103/RevModPhys.81.109).
- [36] U. F. P. Seifert, T. Meng, and M. Vojta, “Fractionalized fermi liquids and exotic superconductivity in the kitaev-kondo lattice,” *Physical Review B*, vol. 97, no. 8, 2018. DOI: [10.1103/physrevb.97.085118](https://doi.org/10.1103/physrevb.97.085118).

## Bibliography

- [37] J. Knolle, S. Bhattacharjee, and R. Moessner, “Dynamics of a quantum spin liquid beyond integrability: The kitaev-heisenberg- $\Gamma$  model in an augmented parton mean-field theory,” *Phys. Rev. B*, vol. 97, p. 134 432, 2018. DOI: [10.1103/PhysRevB.97.134432](https://doi.org/10.1103/PhysRevB.97.134432).
- [38] D. J. Rizzo et al., “Charge-transfer plasmon polaritons at graphene/ $\alpha$ -RuCl<sub>3</sub> interfaces,” *Nano Letters*, vol. 20, no. 12, pp. 8438–8445, 2020. DOI: [10.1021/acs.nanolett.0c03466](https://doi.org/10.1021/acs.nanolett.0c03466).
- [39] C. Küppersbusch and L. Fritz, “Modifications of the lifshitz-kosevich formula in two-dimensional dirac systems,” *Physical Review B*, vol. 96, no. 20, 2017. DOI: [10.1103/physrevb.96.205410](https://doi.org/10.1103/physrevb.96.205410).
- [40] I. N. Yakovkin and P. A. Dowben, “The problem of the band gap in LDA calculations,” *Surface Review and Letters*, vol. 14, no. 03, pp. 481–487, 2007. DOI: [10.1142/S0218625X07009499](https://doi.org/10.1142/S0218625X07009499).
- [41] J. P. Perdew, “Density functional theory and the band gap problem,” *International Journal of Quantum Chemistry*, vol. 28, no. S19, pp. 497–523, 1985. DOI: <https://doi.org/10.1002/qua.560280846>.
- [42] H.-K. Jin and J. Knolle, *Flat and correlated plasmon bands in graphene/ $\alpha$ -rucl<sub>3</sub> heterostructures*, 2021. arXiv: [2103.03941](https://arxiv.org/abs/2103.03941).
- [43] Y. Adamov, I. V. Gornyi, and A. D. Mirlin, “Interaction effects on magneto-oscillations in a two-dimensional electron gas,” *Phys. Rev. B*, vol. 73, p. 045 426, 2006. DOI: [10.1103/PhysRevB.73.045426](https://doi.org/10.1103/PhysRevB.73.045426).
- [44] F. Denef, S. A. Hartnoll, and S. Sachdev, “Quantum oscillations and black hole ringing,” *Phys. Rev. D*, vol. 80, p. 126 016, 12 2009. DOI: [10.1103/PhysRevD.80.126016](https://doi.org/10.1103/PhysRevD.80.126016).
- [45] F. Denef, S. A. Hartnoll, and S. Sachdev, “Black hole determinants and quasinormal modes,” *Classical and Quantum Gravity*, vol. 27, no. 12, p. 125 001, 2010. DOI: [10.1088/0264-9381/27/12/125001](https://doi.org/10.1088/0264-9381/27/12/125001).

# List of Figures

2.1 Schematic depiction of the effect of a magnetic field on the momentum eigenstates in the perpendicular plane. . . . .	4
3.1 Honeycomb lattice and Kitaev–Kondo model . . . . .	14
3.2 Schematic phase diagram of the Kitaev–Kondo model . . . . .	16
3.3 Band structure of the full and the effective Hamiltonian . . . . .	18
3.4 Comparison of the effective band structure and the DFT band structure . . . . .	20
3.5 Magnetization and non-LK amplitude . . . . .	26
3.6 Optical and schematic image of a typical $\alpha$ -RuCl <sub>3</sub> -graphene device . . . . .	28
3.7 Fit of the experimental data and the oscillations of the longitudinal resistance and the magnetization . . . . .	30
3.8 Simultaneous fit of various amplitudes of sample B at different $B$ -fields . . . . .	32
A.1 The two possible integration paths to close the contour. . . . .	44
B.1 Landau Levels of the effective Hamiltonian . . . . .	48
B.2 The Fourier spectra in $B^{-1}$ of the two samples B (a) and C (b) for various temperatures predict clear maxima at $F(B) = 390$ T and $F(C) = 386$ T. . . . .	49
B.3 Same as fig. 3.7 (a) but $\omega_t$ is now a fitting parameter for the LK fits. . . . .	50

## List of Tables

3.1 Fitting parameters and quality criteria of the solid curves in fig. 3.7 and fig. 3.8. . . . .	31
B.1 Fitting parameters and quality criteria of the LK curves (dashed) in fig. 3.7 (a) (first three rows) and fig. B.3 (last three rows). . . . .	50

# Appendix A

## Derivation of the Generalized LK Formula

We start from the generic formula of the great canonical potential of an interacting system

$$\Omega = -T \operatorname{tr}_{l,\omega_n,k_x,\lambda} (\ln -G^{-1}(i\omega_n)) - T \operatorname{tr} (G(i\omega_n)\Sigma) + \Omega' \quad (\text{A.1})$$

as it was stated in eq. [2.15](#).

In the following calculation we will only be interested in terms oscillating with  $1/B$ , all other terms that are constant or just add a slowly varying background are not considered. Note that since we will not include any cut-offs, non-oscillating divergences may appear which can be dropped as well. The oscillating parts of  $\Sigma'$  cancel exactly with  $-T \operatorname{tr} (G(i\omega_n)\Sigma)$  [43](#), such that up to non-oscillatory terms

$$\Omega_{\text{osc.}} = -T \operatorname{tr}_{l,\omega_n,k_x,\lambda} (\ln -G^{-1}(i\omega_n)). \quad (\text{A.2})$$

For convenience we may drop the index *osc.* from now on.

The finite temperature Green's function  $G_l(i\omega_n)^{-1} = i\omega_n - E_{l,\sigma} - \Sigma_{l,\lambda}(i\omega_n)$  will in most cases, which are accessible by analytic calculations, not depend on  $k_x$ , so we may as well assume that. Depending on the interactions, especially beyond the discussed  $\delta$ -like disorder potential,  $\Sigma$  and hence  $G(i\omega_n)$  could become a function of  $k_x$ . In all other cases the sum over  $k_x$  is trivial and gives  $N_\Phi$ . The sum over LLs  $l$  can be transformed with the Poisson resummation formula

$$\sum_{l=0}^{\infty} f_l = \sum_{k=-\infty}^{\infty} \int_0^{\infty} dl e^{2\pi i k l} f(l) \quad (\text{A.3})$$

to a sum over harmonics

$$\Omega = -T N_\Phi \operatorname{tr}_{\omega_n,\lambda} \sum_k \int_0^{\infty} dl e^{2\pi i k l} \ln -G^{-1}(l, i\omega_n). \quad (\text{A.4})$$

The zeroth harmonic is clearly non-oscillating.<sup>[1](#)</sup> Performing integration by parts and

---

<sup>1</sup>This is only true, if the self-energy is non-oscillating. Note that the zeroth harmonic is divergent, since the sum over LLs  $l$  did not have a cut-off initially.

Appendix A Derivation of the Generalized LK Formula

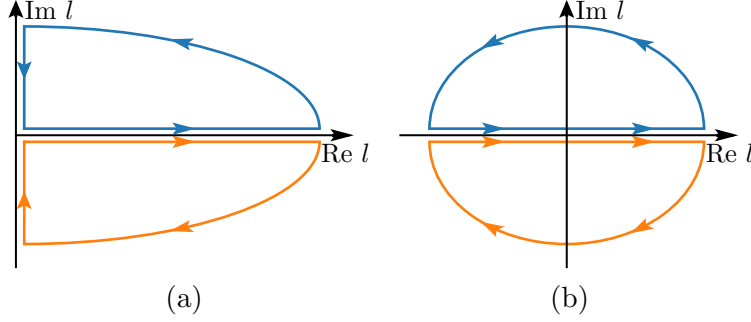


FIGURE A.1: The two possible integration paths to close the contour. In (a) the contour is closed along the imaginary axis, in (b) via extending the left integration border to  $-\infty$ . The blue (orange) paths are for  $k > 0$  ( $k < 0$ ).

using that the boundary terms are non-oscillating as well, we obtain

$$\Omega = TN_{\Phi} \text{tr}_{\omega_n, \lambda} \sum_{k \neq 0} \frac{1}{2\pi i k} \int_0^{\infty} dl e^{2\pi i k l} \frac{\frac{d}{dl} G^{-1}(l, i\omega_n)}{G^{-1}(l, i\omega_n)}. \quad (\text{A.5})$$

The integral can be solved by complex contour integration. We assume that  $G^{-1}(l, i\omega_n)$  has only a single zero of order  $n_{l^*} = 1$  at  $l^*$ .<sup>2</sup> It is important to realize that

$$\text{Res}_{l^*} \left( \frac{\frac{d}{dl} G^{-1}(l, i\omega_n)}{G^{-1}(l, i\omega_n)} \right) = n_{l^*} \quad (\text{A.6})$$

In order to rewrite the integral in terms of the residue, the contour needs to be closed. There are two possible ways to achieve this. The first possibility is to close the contour along the imaginary axis, see fig. A.1 (a), and then argue that the arc does not contribute and the contribution from  $\pm i\infty$  to 0 is non-oscillatory. This has been done previously in ref. [39] for graphene and in ref. [1] for this very calculation.

A different but similar ansatz is to argue that the  $\Re l^*$  is at least of the order of  $\mu/\omega_c$  which is typically large. By shifting the pole to zero the lower boundary of the integral  $\approx -\mu/\omega_c$  can safely be extended to  $-\infty$ . The arc, extending now over two quadrants, does not contribute. This has been done in ref. [19] for quasi two-dimensional metals.

The advantage of the first method is that it does not require a large  $\Re l_n^*$  which may not necessarily be given, especially in systems with Dirac conical band structures at low filling. But in these systems it is questionable, if QOs with such small frequencies can be observed experimentally anyways. The disadvantage is that it is not directly obvious

<sup>2</sup>This condition can easily be relaxed by including the summation over all poles in the tr. The order of the pole becomes a prefactor of the potential.

why the contribution along the imaginary axis is non-oscillatory, since  $G^{-1}(-il, i\omega_n)$  could still be oscillatory.<sup>3</sup> In the supplementary material of ref. [1], it becomes evident that this does not happen.

The only change in the result between the two different approaches is that the appearance of a  $\theta(\Re l^*)$ . The occurrence of a pole with  $\Re l^* < 0$  is however unphysical, since  $l$  usually originates from the eigenstates of the harmonic oscillator and can therefore only take values larger than zero. Hence, the only possibility for  $\Re l^*$  to become smaller than zero is from the self-energy or temperature, quantities which are usually small. In summary it can be stated that for observable QOs the path how the contour is closed does not matter, only small frequencies require more careful treatment.

We follow the first approach to close the contour, the integral then reads

$$\int_0^\infty dl e^{2\pi i k l} \frac{d}{dl} \frac{G^{-1}(l, i\omega_n)}{G^{-1}(l, i\omega_n)} = 2\pi i \operatorname{sgn}(k) e^{2\pi i k \operatorname{sgn}(k) l^*} \theta(k \Im l^*) \theta(\Re l^*) \quad (\text{A.7})$$

leading to the grand canonical potential

$$\Omega = T N_\Phi \operatorname{tr}_\lambda \sum_{n, k > 0} \frac{1}{k} e^{2\pi i k l^* \operatorname{sgn}(\Im l^*)} \theta(\Re l^*). \quad (\text{A.8})$$

It has been argued previously that in such equations negative Matsubara frequencies lead to the complex conjugated counterpart of the positive Matsubaras [23, 44, 45]. The physical intuition behind this is the following: The  $\Im l^*$  is usually  $\propto \omega_n$  and the imaginary part of the self-energy  $\Sigma$  has the property  $\operatorname{sgn}(\Im \Sigma) = \pm \operatorname{sgn}(\omega_n)$ . Therefore  $\operatorname{sgn}(\Im l^*) = \pm \operatorname{sgn}(\omega_n)$  changes sign when  $n$  changes sign. The final results is

$$\Omega = 2 T N_\Phi \operatorname{tr}_\lambda \Re \sum_{\omega_n > 0, k > 0} \frac{1}{k} e^{2\pi i k l^* \operatorname{sgn}(\Im l^*)} \theta(\Re l^*). \quad (\text{A.9})$$

Note that there is a factor  $\operatorname{sgn}(\Im l_n^*)$  in the exponent and a factor  $\theta(\Re l_n^*)$  in the sum which do not appear in the original formula of [23]. These additional factors allow for poles in the complete complex plane.

In comparison with the result of ref. [23] there is a small ambiguity, i.e. the prefactor of 2 which does not appear in result of ref. [23]. The factor of 2 is a result of reducing the summation over all Matsubara frequencies to a sum over all positive Matsubara frequencies which is also done in ref. [23]. It is unclear why the results are different. However this inconsistency is not important as in all works the prefactor of the oscillations is replaced by an empirical value.

---

<sup>3</sup>To find this simply substitute  $il \rightarrow l$



## Appendix B

### Additional Material for Chapter 3

#### B.1 Sublattice Symmetry Breaking Term

In this section the influence of a sublattice symmetry breaking term  $g \sum_{\lambda, \lambda'} f_{k, \lambda, \sigma}^\dagger \tau_{\lambda, \lambda'}^z f_{k, \lambda', \sigma}$  for the Kitaev layer is evaluated. A sublattice symmetry breaking term can explain the microscopic details of the band structure in the  $\alpha$ -RuCl<sub>3</sub>-graphene heterostructure. The DFT data in fig. [3.3](#) shows, that the Kitaev Dirac cones are actually gapped, due to the lattice mismatch of graphene and  $\alpha$ -RuCl<sub>3</sub>. This can be modeled by introducing a staggered potential  $g$ , taking opposite values at the two sublattices of  $\alpha$ -RuCl<sub>3</sub>. The effective Hamiltonian

$$H_g = H + g \sum_{\lambda, \lambda'} f_{k, \lambda, \sigma}^\dagger \tau_{\lambda, \lambda'}^z f_{k, \lambda', \sigma} \quad (\text{B.1})$$

can be transformed analogously to before to the LL Hamiltonian

$$H_{LL, g} = \sum_{l=1, q_x, \sigma, \zeta} \Psi_{l, q_x, \sigma}^{\zeta \dagger} \begin{pmatrix} W & \omega_t \sqrt{l} & \frac{J}{2} & 0 \\ \omega_t \sqrt{l} & W & 0 & \frac{J}{2} \\ \frac{J}{2} & 0 & g & \omega_K \sqrt{l} \\ 0 & \frac{J}{2} & \omega_K \sqrt{l} & -g \end{pmatrix} \Psi_{l, q_x, \sigma}^{\zeta}. \quad (\text{B.2})$$

However the LLs cannot be determined analytically anymore, but their values are still accessible by numerical calculations. From fig. [B.1](#) it becomes evident that a finite  $g$  only changes the Kitaev LLs locally for small  $l$ . While this will most certainly change the value of the pole  $l_+^*$ , the relevant pole  $l_-^*$  which is located at relatively high LLs  $\Re l_-^* = W^2/\omega_t^2$ , remains unaffected.

Therefore we can think of the quantity  $g$  similar as of the Kitaev cyclotron frequency  $\omega_K$ . Both influence the microscopic band structure, but as long as they stay smaller than a certain threshold they will not influence the found *anomalous QOs*.

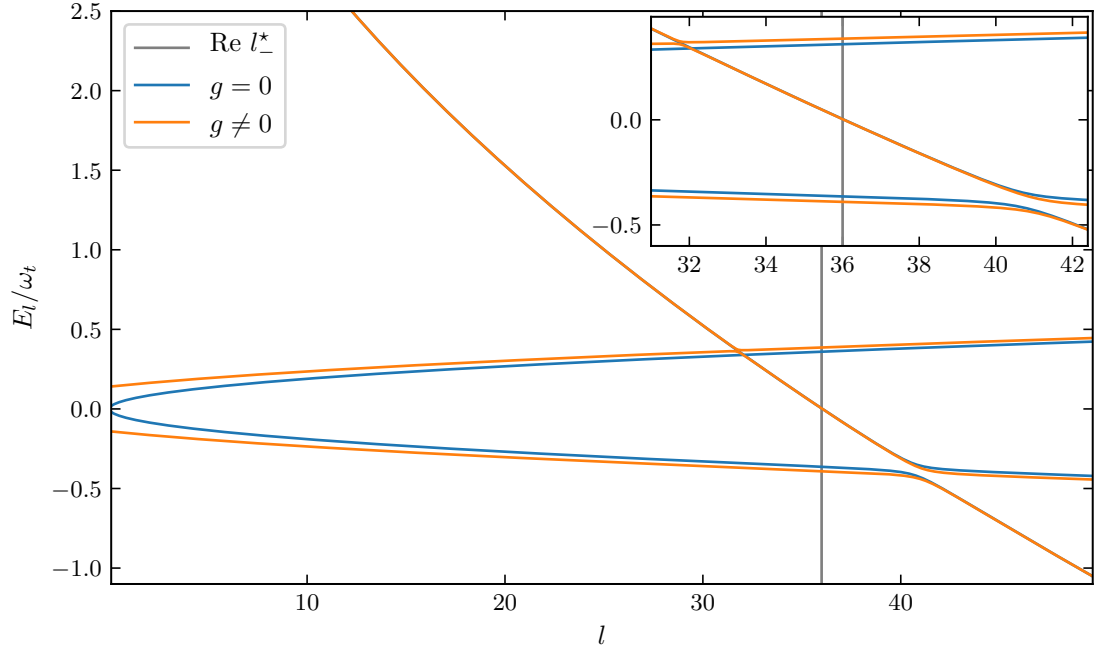
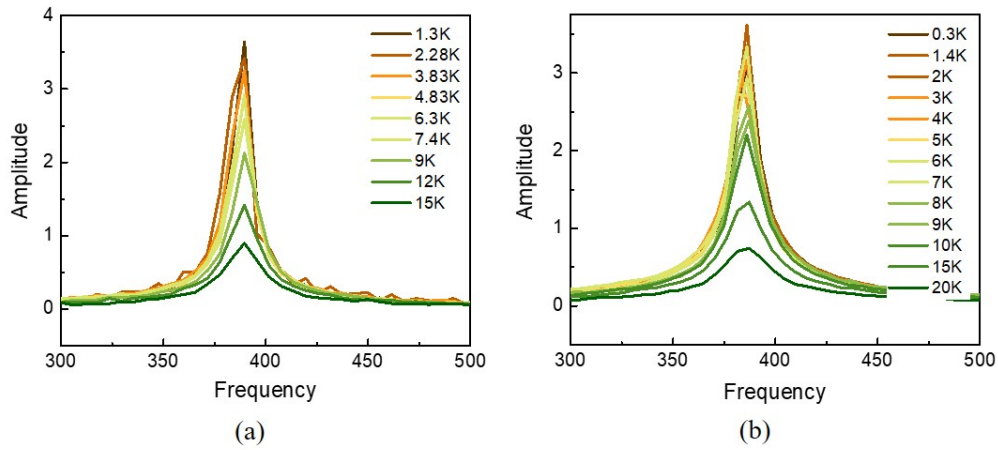


FIGURE B.1: The Landau Levels of the effective Hamiltonian with  $g = 0$  and  $g = 14$  meV and  $l$  is treated as continuous parameter. The gray line is located at the value of  $\Re l_n^*$  for  $B \approx 11$  T. Note that the macroscopic parameters  $W$  and  $\omega_t$  are taken from the  $\alpha$ -RuCl<sub>3</sub>-graphene heterostructure and the microscopic parameters  $\omega_K$ ,  $J$  and  $g$  are artificially increased to visualize their effect on the LLs. The inset shows a zoom-in to the region which is relevant for the QOs.

## B.2 Fourier Spectra of Sample B and C

The Fourier spectra can be obtained by performing a discrete Fourier transformation of the measurement data at equal intervals of  $1/B$ . A Fourier spectrum from sample A is not accessible.



[Reprinted figure with permission from [V. Leeb et al., Phys. Rev. Lett., 126, 097201 2021.] Copyright 2021 by the American Physical Society.]

FIGURE B.2: The Fourier spectra in  $B^{-1}$  of the two samples B (a) and C (b) for various temperatures predict clear maxima at  $F(B) = 390$  T and  $F(C) = 386$  T.

### B.3 Additional Fits and Fitting Parameters

sample	$W$	$\omega_t$	$R^2$	Adj. $R^2$
A	583 meV	96.5 meV	0.95517	0.94620
B	603 meV	104 meV	0.98497	0.98309
C	600 meV	96.5 meV	0.98317	0.98177
A	583 meV	117 meV	0.98201	0.97301
B	603 meV	121 meV	0.99548	0.99418
C	600 meV	110 meV	0.99420	0.99315

TABLE B.1: Fitting parameters and quality criteria of the LK curves (dashed) in fig. 3.7 (a) (first three rows) and fig. B.3 (last three rows).

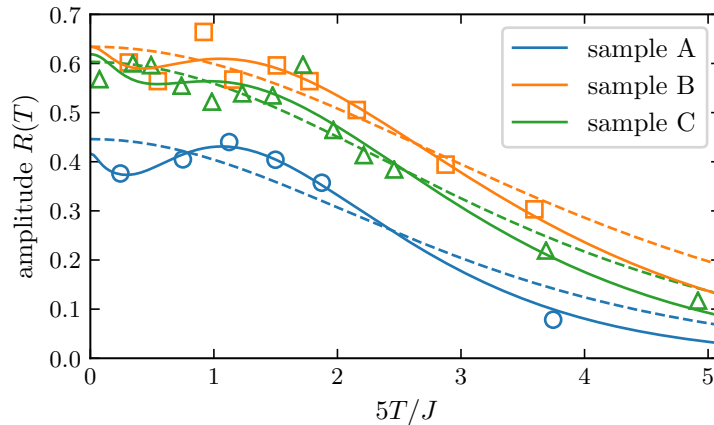


FIGURE B.3: Same as fig. 3.7 (a) but  $\omega_t$  is now a fitting parameter for the LK fits. The LK fits have improved with respect to fig. 3.7 (a) but the values for  $\omega_t$ , see tab. B.1, are at odds with the microscopic values of  $\omega_t$  which are derived from the DFT band structure and the corresponding magnetic field.